remote sensing

MDPI

Article

Characterization and Validation of ECOSTRESS Sea Surface Temperature Measurements at 70 m Spatial Scale

David S. Wethey [1,*], Nicolas Weidberg [2], Sarah A. Woodin [1] and Jorge Vazquez-Cuervo [3]

[1] Department of Biological Sciences, University of South Carolina, Columbia, SC 29208, USA; woodin@biol.sc.edu
[2] Departamento de Biología de Organismos y Sistemas, Universidad de Oviedo, 33006 Oviedo, Spain; weidbergnicolas@uniovi.es
[3] Jet Propulsion Laboratory, California Institute of Technology, Pasadena, CA 91109, USA; jorge.vazquez@jpl.nasa.gov
* Correspondence: wethey@biol.sc.edu

Abstract: The ECOSTRESS push-whisk thermal radiometer on the International Space Station provides the highest spatial resolution temperature retrievals over the ocean that are currently available. It is a precursor to the future TRISHNA (CNES/ISRO), SBG (NASA), and LSTM (ESA) 50 to 70 m scale missions. Radiance transfer simulations and triple collocations with in situ ocean observations and NOAA L2P geostationary satellite ocean temperature retrievals were used to characterize brightness temperature biases and their sources in ECOSTRESS Collection 1 (software Build 6) data for the period 12 January 2019 to 31 October 2022. Radiometric noise, non-uniformities in the focal plane array, and black body temperature dynamics were characterized in ocean scenes using L1A raw instrument data, L1B calibrated radiances, and L2 skin temperatures. The mean brightness temperature biases were −1.74, −1.45, and −1.77 K relative to radiance transfer simulations in the 8.78, 10.49, and 12.09 µm wavelength bands, respectively, and skin temperatures had a −1.07 K bias relative to in situ observations. Cross-track noise levels range from 60 to 600 mK and vary systematically along the focal plane array and as a function of wavelength band and scene temperature. Overall, radiometric uncertainty is most strongly influenced by cross-track noise levels and focal plane non-uniformity. Production of an ECOSTRESS sea surface temperature product that meets the requirements of the SST community will require calibration methods that reduce the biases, noise levels, and focal plane non-uniformities.

Keywords: ECOSTRESS; SST; validation; calibration

check for updates

Citation: Wethey, D.S.; Weidberg, N.; Woodin, S.A.; Vazquez-Cuervo, J. Characterization and Validation of ECOSTRESS Sea Surface Temperature Measurements at 70 m Spatial Scale. *Remote Sens.* **2024**, *16*, 1876. https://doi.org/10.3390/rs16111876

Academic Editor: Chung-Ru Ho

Received: 8 April 2024
Revised: 16 May 2024
Accepted: 22 May 2024
Published: 24 May 2024

1. Introduction

High spatial resolution sea surface temperature (SST) observations are of great importance for the understanding and modeling of air-sea coupling, ocean dynamics in fronts, upwelling zones, current separation zones, and coasts. The pixel sizes of the operational instruments retrieving satellite SST range from 750 to 1100 m on polar satellite instruments (VIIRS, MODIS, AVHRR, SLSTR) and 2000 to 3000 m on geostationary satellite instruments (ABI, AHI, SEVIRI). Although they can retrieve SSTs in cloudy conditions, microwave sensors have lower spatial resolutions of 25 km. The satellite spatial scales can resolve large-scale patterns, but the fine structure and the underlying filamentous structure of ocean temperature fields are not resolvable with these instruments. All of these platforms suffer from land contamination of coastal pixels due to the complexity of coastlines, which, in some cases, makes it impossible to retrieve SST in upper regions of estuaries and fjords. In addition, in areas with large tidal amplitudes, coastal sediments and rock benches are aerially exposed during low tides (lunar semidiurnal tide period = 12.42 h) that are not synchronous with respect to polar satellite overpass times (period = 12 h), so on days when satellite overpasses coincide with low tide coastal SST retrievals are contaminated by land and on other days with overpasses during high tide they are not contaminated. Geostationary satellites retrieve SST at 15 min to 1 h intervals, so the tidal effects can be compensated, but the pixel sizes (2–3 km) are so large that processes close to the coast are not spatially resolvable. For all of these reasons, there are great advantages to an instrument that has ~10× the resolution of operational SST sensors and that revisits at many different times of day.

For climate change studies, the target accuracy of satellite SST retrievals is 0.1 K, with a stability better than 0.04 K per decade [1–3]. Merchant et al. [4] produced a 1981–2019 climate data record (CDR) with a median uncertainty per individual retrieval of 0.18 K and a long-term stability of −0.026 to 0.004 K/decade from 11 Advanced Very-High-Resolution Radiometer (AVHRR) instruments and 3 Along Track Scanning Radiometers (ATSR). Since the 2000s, median discrepancies between the CDR reanalyzed satellite skin SST and buoys have remained less than 0.1 K [4]. Since 2012, the daily mean difference between VIIRS and drifters has been between −0.1 K and 0.04 K, and robust standard deviations of the difference remain between 0.2 and 0.3 K (SQUAM, [5]). The long-term stability of VIIRS-SNPP is 0.082 K per decade and is 0.068 K per decade for VIIRS-N20 (SQUAM).

The ECOsystem Spaceborne Thermal Radiometer Experiment on Space Station (ECOSTRESS) meets the spatial resolution criteria, but the SST accuracy and stability have not been fully characterized. It was launched on 29 June 2018, and the first scenes were retrieved on 29 July 2018. Pixel size at nadir is 38 × 69 m, but these are resampled to 70 × 70 m. It has five infrared bands centered on 8.29, 8.78, 9.20, 10.49, and 12.09 μm and acquires a cross-track swath approximately 400 km wide. From 15 May 2019 to 17 May 2023, only three bands were active (8.78, 10.49, 12.09 μm). The instrument has black bodies at 293 K and 319 K, which are used to calibrate the sensor radiances on every rotation of the two-sided scan mirror. The cold black body temperature varies because it depends on the coolant loop of the Japan External Module. The hot black body temperature is regulated with heaters, so it is more stable. Because of the inclination and precession of the ISS orbit, ECOSTRESS captures scenes between 51.6°N and 51.6°S, revisit intervals are sub-daily to 5 days, and overpass times vary throughout the day. ECOSTRESS data products include L1B geolocation and satellite view angle data [6], L1B sensor radiances with error estimates [7], L2 land and water surface temperatures and emissivities with error estimates [8], and L2 cloud masks [9]. Between August 2018 and October 2022, more than 311,000 scenes were acquired at an average of 220 per day. Because this is a land mission, the majority of ocean scenes are coastal and include land features.

ECOSTRESS L1B radiance is geolocated and resampled to 70 × 70 m from the original 38 × 69 m pixels. ECOSTRESS L2 surface temperature and emissivity [8] are retrieved from the L1B calibrated sensor radiances with a Temperature Emissivity Separation (TES) algorithm [10,11]. The algorithm was developed for land surface temperature measurements because empirical regression-based split-window methods such as those used operationally over the ocean [12,13] do not work well over unvegetated land surfaces [11], and at the spatial scale and revisit interval of ECOSTRESS observations, surface properties are not known. In TES methods, there are more unknowns than measurements because there are measurements of radiances at the three bands, and the algorithm retrieves three unknown emissivities plus the unknown surface temperature. It is necessary to constrain the additional degree of freedom in order to make the retrieval possible. TES algorithms constrain the emissivities to retain the shape but not the amplitude of the emissivity spectrum [10]. However, over the ocean, true emissivities are much more tightly constrained than those normally retrieved by TES methods, so there is a potential for TES surface temperatures to have greater error variances than values retrieved after constraining emissivity using established relationships among emissivity, 10 m wind speed, satellite viewing angle, and temperature [14–17]. Since surface temperature is related to infrared radiance divided by emissivity, temperature biases over the ocean may arise depending upon the magnitude of the difference between the emissivities retrieved by TES and the emissivities calculated from the sea state. Emissivities with negative biases lead to positive temperature biases and vice versa. Many operational regression-based split-window SST retrieval algorithms [12,13,18,19] bypass the emissivity problem by regressing in situ measurements against sensor radiances, differences among sensor radiances, satellite view angles, and their products to calculate coefficients for retrieval equations.

ECOSTRESS skin temperature retrievals over water have been previously compared to in situ observations from lakes [20,21], coastal buoys [22], and VIIRS SST retrievals [23]. Because ECOSTRESS is primarily a terrestrial mission, no sea surface temperature (SST) product is produced; instead, the land surface temperature (LST) product is generated over both water and land. In order to determine whether the TES algorithm was adequate to produce SST from ECOSTRESS, we carried out an in-flight validation of ECOSTRESS surface temperatures and brightness temperatures over the ocean with quality-controlled data from the NOAA in situ SST Quality Monitor (iQuam, [24]), and with collocated GHRSST Level-2P SST from instruments on geostationary satellites (ABI on GOES-16 and 17 [25,26]; AHI on Himawari-8 [27]; SEVIRI on MSG-1, MSG-2 and MSG-4 [28–30]).

Calibration and validation of the instrument on the ocean have great advantages relative to calibration on land. First, the infrared emissivity of the ocean is much more spatially uniform than that of land surfaces, where fine-scale variation in substratum type can lead to emissivity variation. For example, on the ocean at the maximum ECOSTRESS view zenith angle of 28.34°, the effect of both wind speed and view angle on emissivity at 10.5 μm is ± 0.0005 [14,31], and the effect of temperature on emissivity is less than ± 0.001 [32] (emissivity is a dimensionless quantity that ranges between 0 and 1). By contrast, the emissivities of land surfaces can vary between 0.99 and 0.7, depending on the surface type (vegetation, soils, rocks, sand). Second, the specific heat of water is higher than that of most terrestrial materials, so diurnal changes in temperature (which complicate validation) are smaller. Third, the number of terrestrial validation sites is small, so the number of potential collocations per month is small. By contrast, in the global ocean, there are approximately 7900 platforms (buoys, drifters, moorings, ships), providing more than 2.2 million quality-controlled SST measurements per month to the NOAA in situ SST Quality Monitor [24], so there are vastly more opportunities for collocation than are available on land. There are also 2 km spatial scale ocean skin temperature retrievals available every 15 min from the GHRSST Level 2P archive of data from the Eumetsat geostationary MSG-SEVIRI instruments over the eastern Atlantic and Indian Oceans [28–30,33]. There remain, however, diurnal variations and bulk–skin differences that complicate the validation of SST retrievals [2,34].

1.1. Cloud Masks

Cloud masking is necessary because the TES and operational SST algorithms all require a clear sky. The ECOSTRESS cloud mask was developed for observations over land [35]. It has several tests: Test 1 uses 10.49 μm brightness temperature and surface elevation in km (DEM). Pixels with $BT_{10.49} < 300\ K - 6 \times DEM$ are considered cloudy (over the ocean DEM = 0). Test 2 uses $BT_{10.49} - BT_{12.09} > 6$ to indicate thin clouds and cirrus. Test 3 uses $BT_{8.78} - BT_{10.49} > -1$ to indicate clouds. For the ocean, Test 1 is not appropriate because ocean temperatures are mostly below 300 K.

Because the ECOSTRESS cloud masks underdetect clouds, we used cloud masks from L2 GHRSST geostationary satellite SST files processed by NOAA and archived at podaac.jpl.nasa.gov (accessed on 22 May 2024). The cloud masks for GOES-16, GOES-17, and Himawari-8 were from the NOAA Advanced Clear Sky Processor for Oceans (ACSPO) [12], and the cloud masks for EUMETSAT MSG-01, MSG-02, and MSG-04 were from the NOAA version of the Generalized Bayesian Cloud Screening code from the University of Edinburgh [13]. Geostationary observations were at a much coarser spatial scale (2–3 km) than ECOSTRESS, but because of their sub-hourly to hourly sampling rate, matchups were available for all ECOSTRESS scenes. Polar satellite matchups were far less frequent and were not used in this study.

1.2. Sensor Calibration

The instrument used in ECOSTRESS is the Prototype HyspIRI-TIR (PHyTIR). The detector is a Mercury Cadmium Telluride (HgCdTe) array. HgCdTe detectors have well-defined nonlinearities [36–40], so linear rather than quadratic calibrations may lead to errors. Calibration of HgCdTe sensors on operational missions often uses a quadratic equation, either based on pre-flight measurement of the nonlinearity (AVHRR [40–42], ASTER [39,43,44], SLSTR [45]) or a combination of pre-flight and on-orbit measurements (MODIS [46], VIIRS [47–49]). ECOSTRESS uses a two-point linear calibration for each pixel in the focal plane array on a scan-by-scan basis based on onboard black bodies at 293 K and 319 K [20,50]. Since most ocean temperatures are below the temperature of the cold black body, sensor nonlinearities may be important. Pre-launch coefficients for each detector in the focal plane array were not measured, although the average linearity of the focal plane was measured over a temperature range of 278 to 338 K [51].

1.3. Scan Geometry

ECOSTRESS is a push-whisk instrument with a 256 pixel $\times$ 5 band focal plane array (FPA) with a per-pixel resolution of 38 $\times$ 69 m at nadir, resampled to 70 $\times$ 70 m [52]. Blocks of 16 pixels in the cross-track direction are covered by a set of bandpass filters for the different wavelength bands. Pixels 34–48 of the 12.09 µm region of the FPA are non-responsive, so the missing radiance data are filled with values predicted from the other bands using a machine-learning algorithm [53]. Pixels are binned with their nearest neighbors to provide a 70 m resolution at the nadir and an effective FPA size of 128 pixels and to reduce smearing and optical distortions in the along-track direction [54]. Each rotation of the scanning mirror permits 5400 across track retrievals of the 128-pixel FPA for each band, and there are 44 scans per scene, yielding a raw 5400 $\times$ 5632 image. There are 64 retrievals from each of the two black bodies on each scan, allowing calculation of a per scan gain and offset for each pixel. The circular 230 mm diameter cold black body is scanned perpendicularly, and the 300 mm $\times$ 220 mm warm black body is image scanned at a 45° angle [53]. Adjacent earth scans overlap by approximately 30 pixels. ECOSTRESS L1–L4 data products retain the raw 5400 $\times$ 5632 structure of the scans, including the overlapping regions. For example, pixels 97–128 of the FPA on one mirror scan may overlap pixels 1–30 of the focal plane on the next scan. Because of the orbital motion and yaw of the ISS, the overlaps are not perfect and resemble a Moire pattern. There is also a bowtie effect, with the degree of overlap changing as a function of the view zenith angle.

The NASA/USGS Land Processes Distributed Active Archive Center (LP DAAC) provides a nearest-neighbor resampling tool [55] for projecting the raw scan data onto a UTM or longitude–latitude grid. The spatially shifting pixel overlap creates image artifacts because the nearest neighbor of the ground target location may come from either pixels 1–30 or 97–128 of the focal plane, and that assignment shifts from pixel to pixel, leading to a checkerboard pattern of data from pixels at opposite ends of the focal plane.

1.4. Data Versions

ECOSTRESS Collection 1 uses processing software Build 6 and covers the period from launch to present; it is available at the LP DAAC (https://e4ftl01.cr.usgs.gov/ECOSTRESS, accessed on 22 May 2024). ECOSTRESS Collection 2 uses processing software Build 7, which covers the period 26 October 2022 to present and is available on the USGS Land Processes Cloud (LPCLOUD). Collection 2 radiances differ from Collection 1 radiances by linear gain and offset coefficients derived from matchups to in situ calibration/validation sites [52]. There are plans to reprocess all ECOSTRESS scenes prior to 26 October 2022 with Build 7, but those data were unavailable at the time of writing. All ECOSTRESS data are available without cost and are searchable at https://search.earthdata.nasa.gov (accessed on 22 May 2024).

We largely restricted our analysis to Collection 1 (Build 6) because it has a much longer period of record (9 July 2018 to present) than Collection 2 (Build 7, 26 October 2022 to present). During all but the first 5 months of the period of our analysis, only the 8.78, 10.49, and 12.09 µm bands were active, so we restricted our analyses to those bands.

Because Collection 2 radiance conversion coefficients are available, it was possible to convert Collection 1 radiances to Collection 2 equivalent radiances and brightness temperatures, which allowed for examining brightness temperature biases in both Collection 1 and Collection 2 (Sections 2.3 and 3.3 below).

1.5. Relation to Other Missions

ECOSTRESS has approximately 10× the spatial resolution of operational SST missions like VIIRS and MODIS. It serves as a precursor for future planned 50–60 m scale thermal missions TRISHNA (CNES-ISRO) [56], SBG (NASA) [57], and LSTM (ESA) [58], which together are expected to provide global daily 50–60 m coverage of the ocean within 100 km of the world's coasts. ECOSTRESS and all of these planned instruments have design constraints, so an understanding of the consequences of those limitations will be useful in the development of methods for improving the quality of temperature retrievals.

2. Materials and Methods

2.1. Matchups

Triple collocations [59] were used to match single ECOSTRESS L2 skin temperature pixels to NOAA iQuam in situ observations [60] and to single Level-2 GHRSST L2P SST clear sky pixels from geostationary satellites (GOES-16 [25], GOES-17 [26], Himawari-8 [27], MSG-1 [28], MSG-2 [29], MSG-4 [30]). The ECOSTRESS-iQuam matchups were within 30 min and 100 m, and the ECOSTRESS-geostationary matchups were within 30 min and 1.5 km. All clear sky triple collocations over the period 1 December 2018 to 31 October 2022 were used. Data were separated into day and night subsets.

The data quality variable in iQuam files is "quality_level", and values range from 0 (invalid) to 5 (best quality). The data quality variable in ECOSTRESS L2_LSTE files is "QC" and is an unsigned 16-bit variable; if bit 15 = 1, the LST accuracy is good to excellent. The 8-bit cloud variable in the ECOSTRESS L2_CLOUD files is "CloudMask"; clear sky water pixels are identified by a value of 33 (bit 5 = 1 indicates water pixel, bit 0 = 1 indicates cloud mask was determined, bits 1 to 4 = 0, no clouds detected). We compared matchups between best quality iQuam (quality_level = 5) data and "good to excellent LST accuracy" ECOSTRESS (QC bit 15 = 1) temperature retrievals with no ECOSTRESS clouds (CloudMask = 33). We then made increasingly strict subsets of the data: (1) geostationary SST non-missing, (2) best quality geostationary SST (quality_level = 5), (3) best quality geostationary SST and robust outliers were removed (absolute value of ECOSTRESS bias < median of absolute value of bias + 4 × robust standard deviation). The robust standard deviation (RSD) was calculated as the interquartile range/1.349 [41].

2.2. Observation and Model Brightness Temperatures

ECOSTRESS infrared (IR) band brightness temperatures (BT) at 8.78 µm, 10.49 µm, and 12.09 µm were calculated from L1B calibrated band radiances [7] using the ECOSTRESS brightness temperature lookup tables [61] for the inverse Planck function. Infrared (IR) band brightness temperatures at 8.6 µm, 10.4 µm, and 12.3 µm from the geostationary satellites were obtained from L2P GHRSST data for NOAA GOES-16 [25], and GOES-17 [26] (ABI Instrument), Japan Meteorological Agency Himawari-8 [27] (AHI Instrument). Brightness temperatures were not available in the NOAA-processed L2P GHRSST data for EUMETSAT (European Organisation for the Exploitation of Meteorological Satellites) MSG-1 [28], MSG-2 [29] and MSG-4 [30] (SEVIRI Instrument).

Radiative transfer modeling of channel brightness temperatures was carried out with RTTOV 12.3 [17], using the iQuam observation as the surface temperature and using ECMWF ERA-5 hourly 0.25° reanalysis data [62] for vertical profiles of air temperature and specific humidity, 2 m air temperature, 2 m specific humidity, and 10 m wind speed, all bilinearly interpolated in space to the iQuam coordinates and linearly interpolated in time to the ECOSTRESS scene time. The K (Jacobian) model was used to calculate atmospheric absorption, sea surface emissivity, and at-sensor brightness temperatures in conjunction with RTTOV coefficient files for ECOSTRESS and the ABI and AHI geostationary satellite instruments. Sea surface emissivity in RTTOV was modeled by the IREMIS algorithm [17,63], which includes the effects of 10 m wind speed, satellite view angle, and in situ surface temperature.

2.3. Bias Analysis

Retrieved skin temperature bias was calculated as ECOSTRESS LST—iQuam in situ temperature. Wind speed influences on bulk–skin temperature differences and skin temperature bias [2,34,64] were examined by regression analysis, using hourly 0.25° ERA-5 10 m winds interpolated bilinearly in space and linearly in space to the collocation coordinates. Nonlinearities in the relationship between skin temperature bias and iQuam temperature were examined by comparing linear and quadratic fits to the data.

The ECOSTRESS emissivity retrievals were compared to RTTOV emissivity calculations at each of the triple collocation sites. Skin temperatures were approximated with iQuam in situ observations, and zenith angles were obtained from the ECOSTRESS L2_GEO files. Emissivity bias was calculated as ECOSTRESS TES emissivity–RTTOV-simulated emissivity at 8.78 μm, 10.49 μm, and 12.09 μm.

Brightness temperature observation-model bias was calculated as ECOSTRESS BT–RTTOV-simulated BT at 8.78 μm, 10.49 μm, and 12.09 μm. Relationships between brightness temperature bias and iQuam temperature were examined by linear and quadratic regression, as were relationships between brightness temperature bias and view zenith angle.

ECOSTRESS Collection 2 applies a linear gain and offset to the channel radiances to correct the Collection 1 biases [52] (8.78 μm: gain = 0.9429, offset = 0.5110; 10.49 μm: gain = 0.9507, offset = 0.5208; 12.09 μm: gain = 0.9448, offset = 0.5515). These gains and offsets were used to convert ECOSTRESS Collection 1 radiances to ECOSTRESS Collection 2 equivalent radiances, which were converted to Collection 2 equivalent brightness temperatures with the ECOSTRESS brightness temperature lookup tables [61]. Collection 2 brightness temperature observation-model bias was calculated as Collection 2 equivalent BT–RTTOV-simulated BT as described above. Robust central tendencies were measured as medians and robust standard deviations (RSD) were measured as the interquartile range/1.349 [41]. Conversion of retrieved LST to its Collection 2 equivalent was not possible because it requires running the TES algorithm for which we do not have the source code or binaries. Only a small subset of our data record has been updated to Collection 2 as of the writing of this paper.

Relationships between retrieved skin temperature bias (LST—iQuam in situ) and retrieved emissivity bias (TES emissivity–RTTOV simulated emissivity) were examined by linear regression. Because of the inverse relationship between emissivity and infrared radiance, we expected a negative relationship between emissivity bias and retrieved temperature bias.

2.4. Sensor Stability

All sensors suffer from drift, so it is important to estimate on-orbit sensor stability. A frequently used method to compare consistency among platforms is double differencing [65]. In this method, one platform is defined as the reference (REF), and the other is the satellite under consideration (SAT). Radiance transfer modeling by RTTOV was used to simulate the brightness temperatures of the reference and satellite. Observation-model brightness temperature double differences were calculated by comparing ECOSTRESS observation-model bias at 8.78 μm, 10.49 μm, and 12.09 μm to geostationary ABI/AHI observation-model bias at 8.6 μm, 10.4 μm, and 12.3 μm. The brightness temperature double difference is defined as

$$DD_{SAT\text{-}REF} = (OBS_{SAT} - MOD_{SAT}) - (OBS_{REF} - MOD_{REF}) \tag{1}$$

where OBS are observed brightness temperatures and MOD are simulated brightness temperatures [65]. The slope of the regression of monthly mean double differences with respect to time was used as a measure of the stability of the sensor calibration.

2.5. Focal Plane Uniformity (Spatial Noise)

We examined focal plane array (FPA) uniformity in images by comparing radiances among pixels in the FPA at the scale of individual focal plane retrievals within cross-track swaths (5400 retrievals per swath). Scenes were masked to retain only ocean pixels. Radiance anomalies for each cross-track retrieval were calculated relative to the mean of the FPA values in the retrieval. Mean anomalies were compared among scenes of ocean surfaces with temperatures ranging from 271.4 K to 301.8 K.

We also compared FPA uniformity in ocean radiance retrievals to FPA uniformity in black body radiance retrievals and black body digital numbers from the same scene. This provides a measure of the effectiveness of the gain and offset calibration method.

2.6. Detector Noise (Temporal Noise)

The ECOSTRESS sensor noise-equivalent delta temperatures (NEdT) measured before launch were 0.13 K, 0.10 K, and 0.29 K for the 8.78 µm, 10.49 µm, and 12.09 µm channels, respectively, at scene temperatures of 25 °C [21]. These channel noise levels may contribute to retrieved surface temperatures in several ways. Since the 10.49 µm channel is the most important in surface temperature retrieval, we expect noise levels in surface temperatures to be similar to the NEdT levels for that channel. In addition, the difference between the 10.49 µm and 12.09 µm channel brightness temperatures is a measure of atmospheric attenuation of IR radiation; thus, we expect an additional contribution of the combined variability of the two channels to the retrieved temperature [66]. In order to estimate noise in the retrieved surface temperature, we calculated successive differences on cross-track transects over ocean pixels. Successive differences effectively de-trend the temperature data, and the median absolute deviation (MAD) among the differences serves as a measure of noise in the signal [67]. The MAD/0.6745 is a robust measure of the standard deviation of the noise, which should be similar to the NEdT.

2.7. Statistics

All calculations were carried out with R version 4.2.3 [68] in the RStudio environment [69]. Data ingest was carried out with packages ncdf4 [70], rhdf5 [71], sys [72], getPass [73], httr [74], purrr [75], rvest [76], dplyr [77], abind [78], udunits2 [79], retry [80], terra [81]. Matchups and masking were calculated with packages RANN [82], sp [83], spatstat [84], bitops [85]. Statistical quantities were calculated using packages stats [68], gslnls [86], jointseg [87], DescTools [88]. Graphics were produced with packages ggplot2 [89], viridis [90], ggpubr [91].

3. Results

3.1. Matchups

Between 12 January 2019 and 31 October 2022, we obtained 237,711 matchups. After robust outlier removal (see below), 35,871 of these were collocated among "good to excellent" quality ECOSTRESS cloud-free ocean observations, "best quality" (quality 5) iQuam in situ observations, and "best quality" (quality 5) geostationary SST retrievals spread over 830 dates. To test the efficacy of the ECOSTRESS cloud mask, we examined the bias of the ECOSTRESS temperature retrievals and iQuam in situ observations. When only the ECOSTRESS cloud mask was applied, there was a large number of retrievals over clouds, leading to a large root mean square error (RMSE) (3.741 K) (Figure 1A). When both the ECOSTRESS and the geostationary cloud masks were used, the number of cloudy retrievals was reduced, and the RMSE was lower (2.871 K) (Figure 1B). After robust outlier removal (absolute value of ECOSTRESS bias < median absolute value of bias + 4 × interquartile range/1.349), RMSE was 0.57 K (Figure 2A), larger than for AVHRR (0.39 K), VIIRS (0.25 K) and MODIS (0.25 K) [5,92].

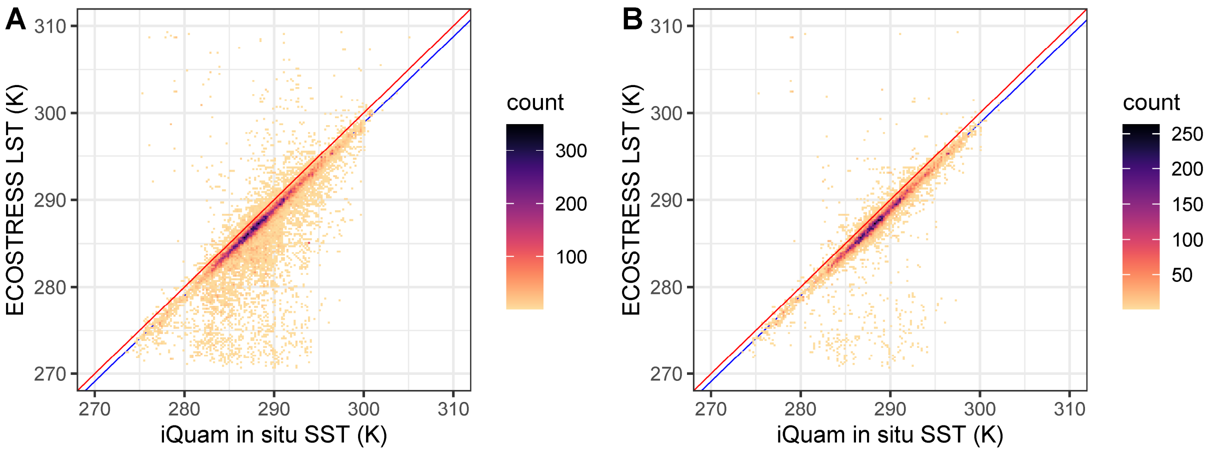

Figure 1. Effect of cloud masks on ECOSTRESS bias: (**A**) ECOSTRESS cloud mask only (RMSE = 3.741 K); (**B**) ECOSTRESS and geostationary cloud masks (RMSE = 2.871 K). Red line is 1:1; blue line is linear regression.

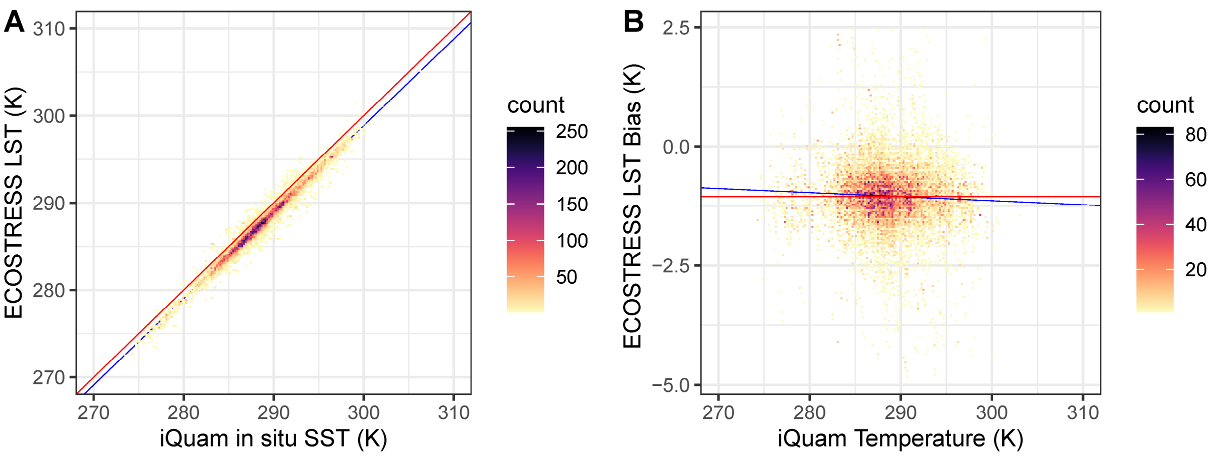

Figure 2. (**A**) Relationship between iQuam in situ SST and ECOSTRESS L2 skin temperature with geostationary cloud mask and robust outlier removal (R^2 = 0.9872, RMSE = 0.567 K). Colors represent number of observations; red line is 1:1; blue line is linear regression. (**B**) Relationship between iQuam in situ SST and ECOSTRESS skin temperature bias; horizontal red line = median bias; blue line is linear regression.

3.2. Bias Analysis

ECOSTRESS L2 skin temperature is strongly correlated with iQuam in situ SST (Figure 2A, R^2 = 0.9782, RMSE = 0.567 K, slope = 0.992, intercept = 1.411, $p < 0.001$). The skin temperature bias had a weak but statistically significant correlation with in situ temperature (Figure 2B, R^2 = 0.0033, slope = −0.00849, $p < 0.001$) and had a median of −1.05 K.

In a subset of the data, which included only collocations with L2P skin temperature retrievals from the Eumetsat geostationary SEVIRI instrument [28–30,33] (N = 1785), ECOSTRESS bias relative to SEVIRI skin temperature was −1.010 K (RSD = 0.556 K), and ECOSTRESS bias relative to iQuam in situ SST was −1.090 K (RSD = 0.415 K). The difference between these two values is a measure of the contribution of the bulk–skin temperature difference to the ECOSTRESS bias relative to iQuam in situ SST.

Wind speed reduces bulk–skin temperature differences [34,64]. There was a weak but statistically significant relationship between skin temperature bias and ERA-5 reanalysis 10 m wind speed, which was linear and negative during daytime (Figure 3A,

R^2 = 0.0054, RMSE = 0.556 K, slope = −0.0134, intercept = −0.8934, N = 24454, $p < 0.001$) and positive during nighttime (Figure 3B, R^2 = 0.0233, RMSE = 0.473 K, slope = 0.0245, intercept = −1.2822, N = 13007, $p < 0.001$). There was no statistical difference between the linear relationship during nighttime and the nonlinear Donlon et al. [64] relationship, which predicted smaller biases at higher wind speeds (Figure 3B). The asymptote of the nonlinear Donlon relationship was −1 K at night (Figure 3B), indicating that the bias is larger than can be explained by the bulk–skin temperature difference, which has an asymptote of −0.13 K at wind speeds above 10 m s^{-1} [34].

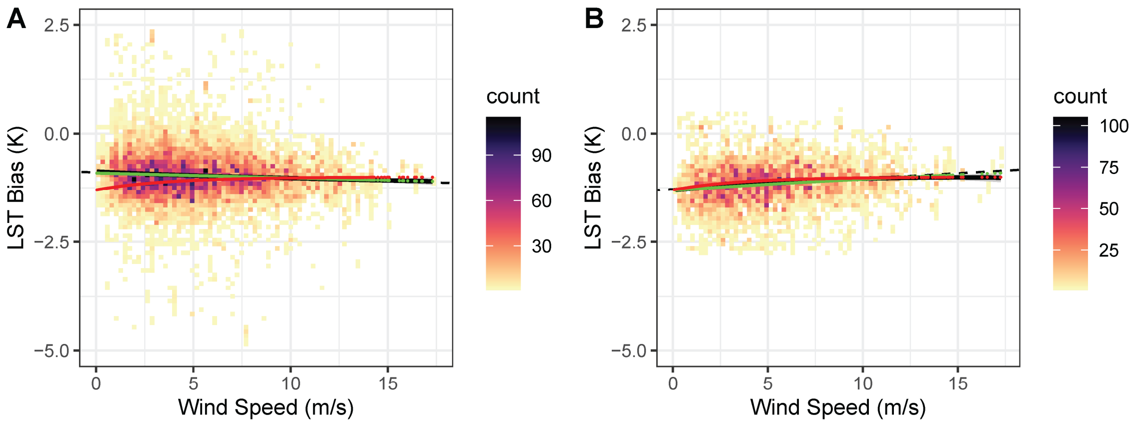

Figure 3. Relationship between ECOSTRESS skin temperature bias and ERA-5 reanalysis wind speed: (**A**) daytime; (**B**) nighttime. Colors represent number of observations: dashed black line—linear fit; solid black line—Loess fit; green line—nonlinear fit; red line—Donlon nonlinear relationship.

ECOSTRESS skin temperature bias is consistently negative with little seasonal or latitudinal influence (Figure 4). The most extreme monthly biases occur in months with low sample sizes. Biases were not plotted when there were less than five collocations per month in a latitude bin.

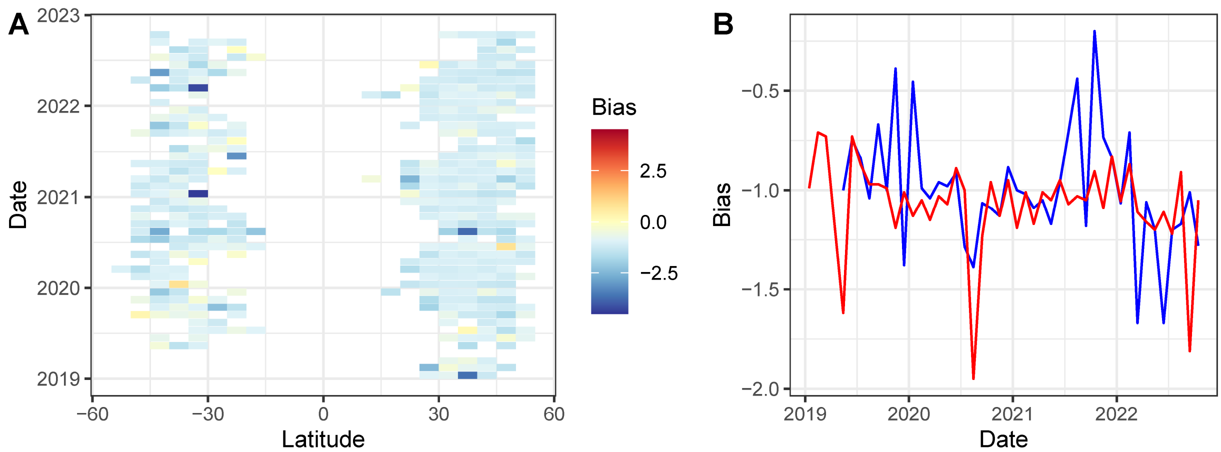

Figure 4. Latitude and date dependence of ECOSTRESS skin temperature bias. Bias was calculated as ECOSTRESS skin temperature—iQuam in situ temperature. (**A**) Colors represent monthly median bias in latitude bins: (**B**) red line = northern hemisphere median bias; blue line = southern hemisphere median bias.

The ECOSTRESS skin temperature uncertainty statistic provided in the ECOSTRESS L2 LSTE files (LST_err) is derived from the TES algorithm [10] and under-estimates the actual error, which is quantified by the absolute value of the skin temperature bias. The actual median skin temperature error relative to in situ observations is 1.05 K, and the range of errors is between 0 and 4.83 K, yet the median of the calculated uncertainty values (LST_err) is 0.92 K, and its range is between 0.56 and 1.48 K.

The ECOSTRESS clear sky brightness temperatures (BT) are lower than those simulated by temperature relative to RTTOV. The median bias of the ECOSTRESS Collection 1 brightness temperature relative to RTTOV and its robust standard deviation (RSD) at 8.78 µm was −1.74 K (RSD = 0.53 K), the median bias at 10.49 µm was −1.45 K (RSD = 0.35 K), and the median bias at 12.09 µm was −1.77 K (RSD = 0.57 K) (Figure 5, red histograms). ECOSTRESS Collection 1 radiances were converted to Collection 2 equivalent radiances and brightness temperatures using the published gains and offsets [52], and biases relative to RTTOV were calculated (Section 2.3). The ECOSTRESS Collection 2 brightness temperature biases (8.78 µm: median bias = −1.01 K, RSD = 0.50 K, 10.49 µm: median bias = −0.84 K, RSD = 0.39 K, 12.09 µm: median bias = −1.21 K, RSD = 0.62 K) are smaller than Collection 1 biases (Figure 5, blue histograms).

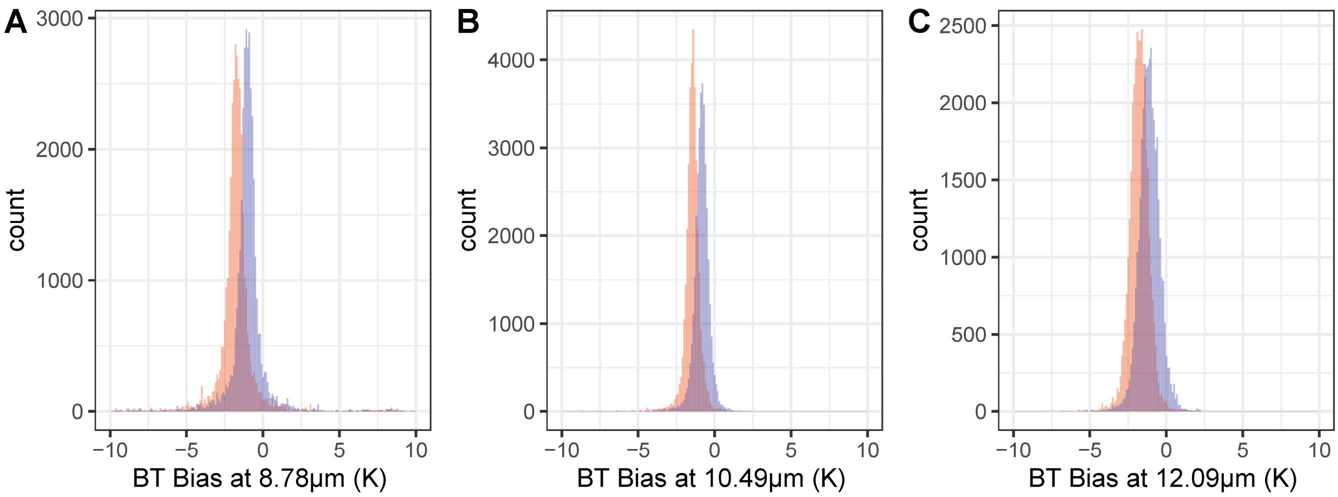

Figure 5. Clear sky brightness temperature (BT) bias distributions: (**A**) 8.78 µm, (**B**) 10.49 µm, (**C**) 12.09 µm. BT bias was calculated as $BT_{ECOSTRESS} - BT_{RTTOV}$. Red: Collection 1; Blue: Collection 2.

Quadratic terms in the relationship between brightness temperature bias and in situ temperature were used as indicators of the nonlinearity of the HgCdTe detectors in the focal plane array. Brightness temperature bias at 8.78 µm had a weak but statistically significant negative quadratic relationship to in situ temperature (Figure 6A: $BTbias_{8.78\mu m} = -3.073 + 2.110 \times iQuam - 0.003 \times iQuam^2$, $R^2 = 0.0046$, RMSE = 1.40 K, $p < 0.001$, N = 35,375). Brightness temperature bias at 10.49 µm also had a weak but statistically significant negative quadratic relationship to in situ temperature (Figure 6B: $BTbias_{10.49\mu m} = -0.0105 + 0.7127 \times iQuam - 0.00122 \times iQuam^2$, $R^2 = 0.0046$, RMSE = 0.537 K, $p < 0.001$, N = 37,449). Brightness temperatures at 12.09 µm had a weak but statistically significant positive quadratic relationship to in situ temperature (Figure 6C: $BTbias_{12.09\mu m} = 0.0202 - 1.380 \times iQuam + 0.00234 \times iQuam^2$, $R^2 = 0.042$, RMSE = 0.641 K, $p < 0.001$, N = 37,449).

Brightness temperature bias at 8.78 µm had a weak positive correlation to view zenith angle (VZA) ($BTbias_{8.78\mu m} = -1.856 + 0.0133 \times VZA$, $R^2 = 0.0025$, $p < 0.001$, RMSE = 1.99 K, N = 37,450). Brightness temperature bias at 10.49 µm was very weakly negatively related to VZA ($BTbias_{10.49\mu m} = -1.461 - 0.00056 \times VZA$, $R^2 = 0.00006$, $p < 0.001$, RMSE = 0.54 K, N = 37,450). Brightness temperature at 12.09 µm had a negative linear and a weak positive quadratic relationship to VZA ($BTbias_{12.09\mu m} = -1.798 - 0.0162 \times VZA + 0.00087 \times VZA^2$, $R^2 = 0.217$, $p < 0.001$, RMSE = 0.65 K, N = 37,450).

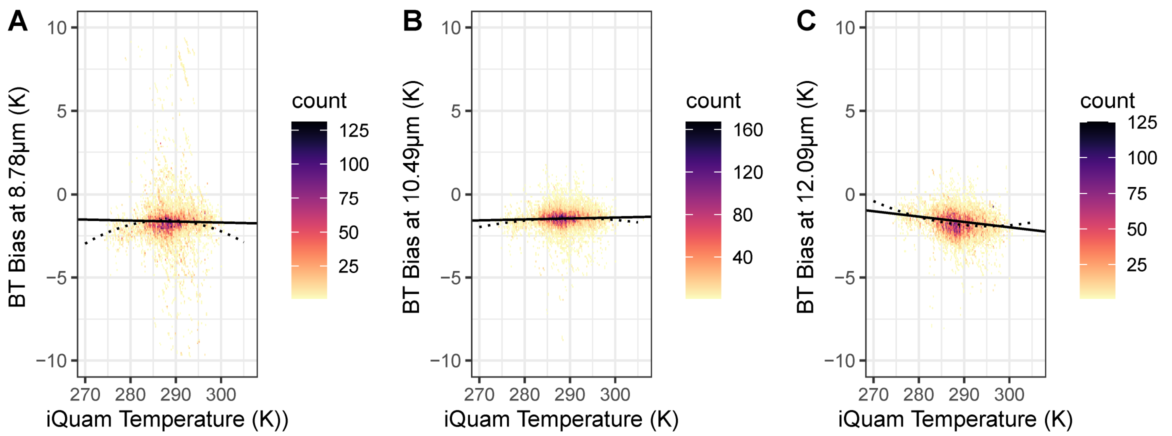

Figure 6. Clear sky ECOSTRESS brightness temperature (BT) bias at 8.78 µm (**A**), 10.49 µm (**B**), and 12.09 µm (**C**) relative to RTTOV temperature. BT bias was calculated as $BT_{ECOSTRESS} - BT_{RTTOV}$. Colors indicate the number of observations. Solid lines are linear regressions; dotted lines are quadratic regressions.

3.3. Emissivity Bias

There was little overlap in the emissivities retrieved by TES (Figure 7, blue histograms) and those estimated by the RTTOV radiance transfer simulations (Figure 7, red histograms). The median 8.78 µm emissivities retrieved by TES (median = 0.966, RSD = 0.0889) were lower than those calculated by RTTOV (median = 0.984, RSD = 0.000), and more than 90% were lower than laboratory [93] emissivity measurements. The 10.49 µm emissivities retrieved by TES (median = 0.982, RSD = 0.003) were all lower than RTTOV emissivities (median = 0.991, RSD = 0.000) and lower than the laboratory measurements of emissivity. More than 90% of 12.09 µm TES emissivities (median = 0.968, RSD = 0.0089) were lower than RTTOV emissivities (median = 0.984, RSD = 0.0014) and the laboratory measurements of emissivity (Figure 7). The distribution of median RTTOV emissivities is within 0.004 of the laboratory spectrum and the variabilities around the RTTOV values are very small ($RMSE_{8.78\mu m}$ = 0.0005, $RMSE_{10.49\mu m}$ = 0.0005, $RMSE_{12.09\mu m}$ = 0.0009), whereas the median TES emissivities relative to RTTOV emissivities are low by 0.009 to 0.018 and the variabilities are much larger ($RMSE_{8.78\mu m}$ = 0.0153, $RMSE_{10.49\mu m}$ = 0.0079, $RMSE_{12.09\mu m}$ = 0.0140) (Figure 7).

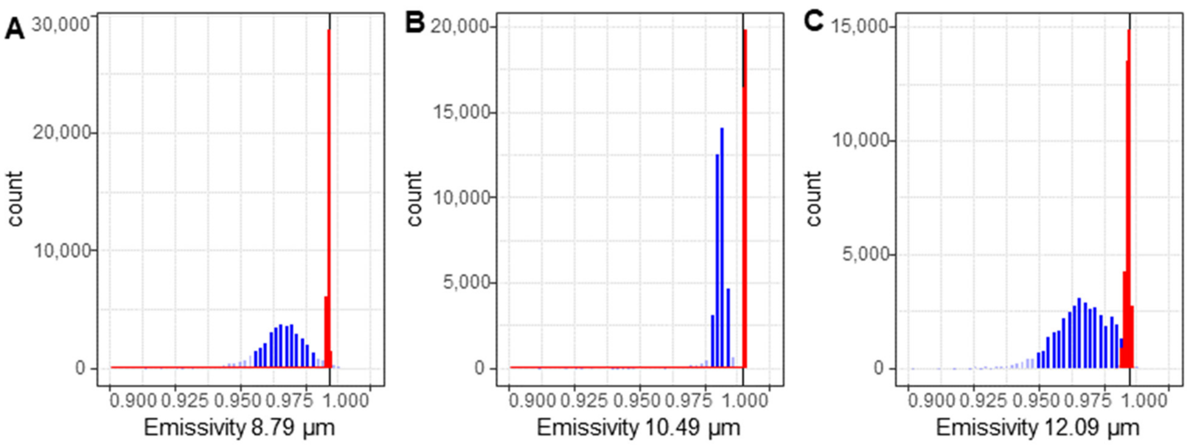

Figure 7. Clear sky sea surface emissivity distributions at 8.78 µm (**A**), 10.49 µm (**B**), and 12.09 µm (**C**) retrieved by TES (blue) and simulated using sea state by RTTOV (red). Vertical black line indicates laboratory measurement of seawater emissivity [57].

Estimates of emissivity uncertainty from the TES algorithm [10] at 8.78 µm (median = 0.0170, RSD = 0.00178), 10.49 µm (median = 0.0128, RSD = 0.00074), and 12.09 µm (median = 0.0101, RSD = 0.00015) differ in magnitude or dispersion or both from the actual emissivity errors at 8.78 µm (median = 0.0171, RSD = 0.00741), 10.49 µm (median = 0.009, RSD = 0.00148), and 12.09 µm (median = 0.017, RSD = 0.01037) (Figure 8). Emissivity uncertainty is defined in the algorithm theoretical basis document as the difference between lab emissivity and retrieved emissivity, which depends upon view angle, total atmospheric column water, and instrument noise [10].

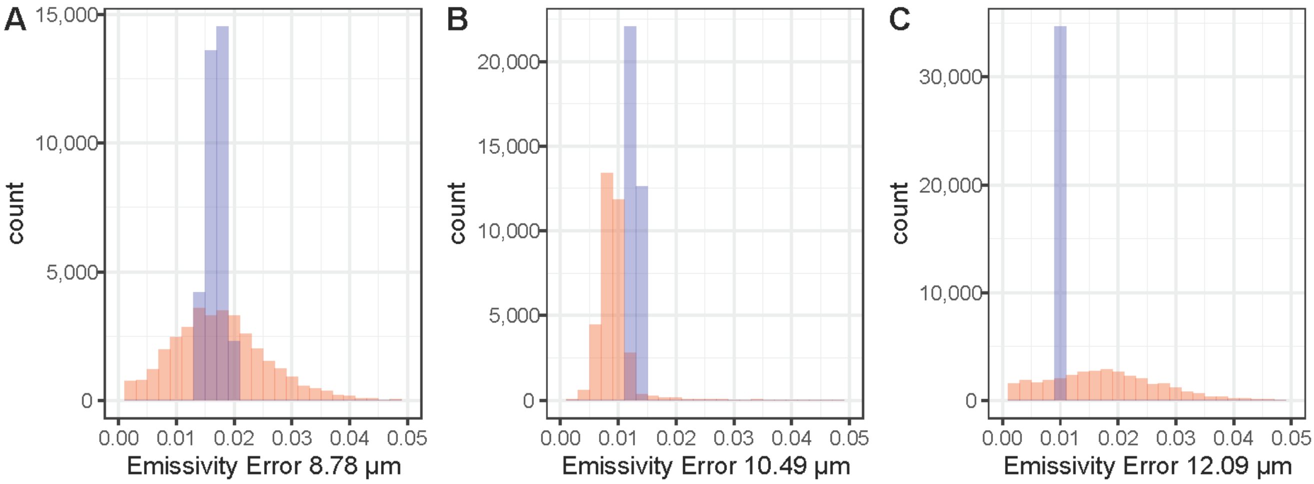

Figure 8. Clear sky emissivity error magnitudes at 8.78 µm (**A**), 10.49 µm (**B**), and 12.09 µm (**C**) predicted by the TES algorithm (blue) compared to the absolute value of TES emissivity bias relative to RTTOV (red).

We expected a negative relationship between emissivity bias and retrieved temperature bias because of the inverse relationship between emissivity and infrared radiance. As expected, the relationship between emissivity bias (TES relative to RTTOV radiance transfer simulations) and skin temperature bias (LST determinations relative to in situ iQuam observations) was negative in all cases (Figure 9). The slope of the relationship was −15.71 in relation to emissivity bias at 8.78 µm ($R^2 = 0.0567$, $p < 0.001$, N = 37,453), −17.31 in relation to emissivity bias at 10.49 µm ($R^2 = 0.0244$, $p < 0.001$, N = 37,453), and −6.77 in relation to emissivity bias at 12.09 µm ($R^2 = 0.0148$, $p < 0.001$, N = 37,453). These regression slopes indicate that for a 0.01 reduction in retrieved emissivity at 8.78, 10.49, and 12.09 µm, the median ECOSTRESS skin temperature bias approached closer to zero by 0.157 K, 0.173 K, and 0.068 K, respectively (Figure 9).

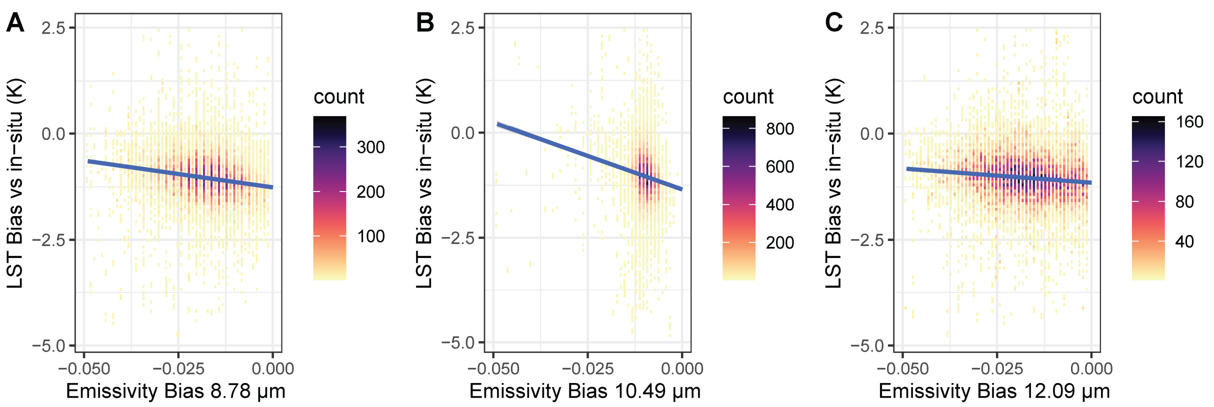

Figure 9. Relationship between emissivity bias (TES relative to RTOVV radiance transfer simulations) and skin temperature bias (LST vs. in situ)=: (**A**) 8.78 µm; (**B**) 10.49 µm; (**C**) 12.09 µm. Blue lines are linear regressions.

3.4. Sensor Stability

Double differences of observation–RTTOV radiance transfer model brightness temperatures were regressed against time to determine the relative temporal stability of the ECOSTRESS instrument compared to the ABI/AHI sensors on geostationary satellites (Figure 10). Double differences were calculated as (ECOSTRESS observation − RTTOV ECOSTRESS simulation) − (ABI observation − RTTOV ABI simulation). The slope of the regression for the 8 µm channel was not significantly different from zero (slope = −0.1169 K/year, p = 0.186, N = 709). The slopes for the 10 µm and 12 µm channels were significantly negative (10.49 µm, slope = −0.1059 K/year, p < 0.001, N = 709; 12.09 µm, slope = −0.1498 K/year, p < 0.001, N = 709) (Figure 10). There was a cold bias relative to RTTOV radiance transfer simulations on all three ECOSTRESS channels relative to the geostationary channels. The median double difference was −0.201 K at 8 µm (RSD = 1.2106 K); at 10 µm, the median value was −0.446 K (RSD = 0.7621 K), and at 12 µm, it was −0.399 K (RSD = 1.1380 K).

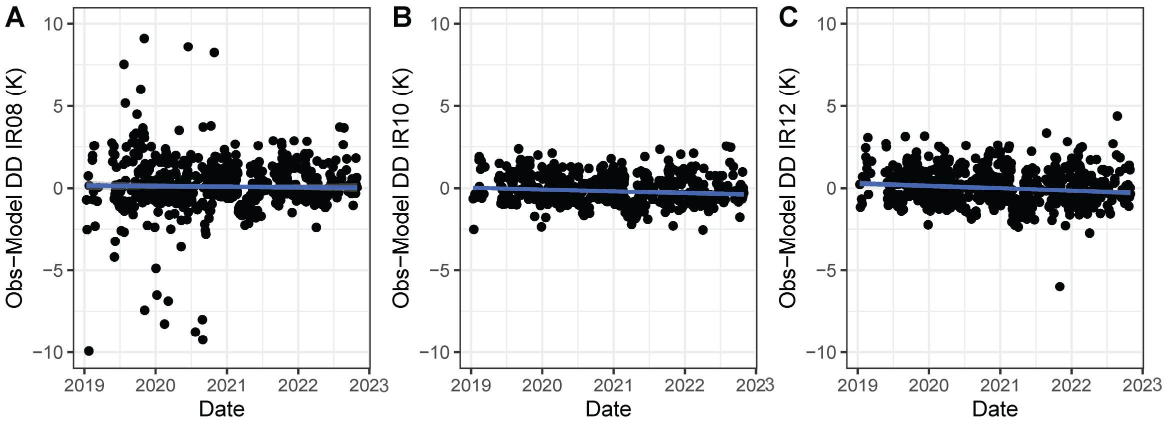

Figure 10. Temporal changes in double differences of observations − RTTOV brightness temperatures. Double differences were calculated as (ECOSTRESS observation − RTTOV ECOSTRESS simulation) − (ABI observation − RTTOV ABI simulation): (**A**) 8 µm; (**B**) 10 µm; (**C**) 12 µm. Blue lines are linear regressions.

3.5. Focal Plane Detector Radiometric Noise (Temporal Noise)

Focal plane detector radiometric noise levels were measured in ocean scenes from the Sea of Okhotsk, the English Channel, Australia, and the Arabian Gulf, with mean SST of 271.4, 279.7, 291.0, and 301.8 K, respectively. Mean cross-track successive differences in brightness temperature varied with scene temperature and among pixels in the focal plane array (Figure 11). The estimates of NEdT by cross-track successive differences were in the same rank order as pre-flight measurements in the laboratory [51], and noise levels varied inversely with scene temperature (Figure 11). However, noise levels in the middle of the focal plane array were substantially greater than the pre-flight values for the 8.78 and 10.49 µm bands (Figure 11A,B). There was also an eight-pixel periodicity in the magnitude of the noise level. In the lowest temperature scene (271.4 K), individual pixels 32, 40, 48, 56, 64, 72, 80, 88, and 96 in the 8.78 µm band had noise levels between 0.28 and 0.32 K, which are between 42 and 62 percent larger than the interpolated pre-flight value of 0.197 K (Figure 11A). Noise levels between those peaks in the 8.78 µm band were somewhat smaller (0.25 to 0.275 K). In the 10.49 µm band, pixels 48, 56, 64, 72, 80, 88, and 96 had noise levels between 0.20 K and 0.23 K in the 271.4 K scene, which are between 21 and 39 percent larger than the interpolated pre-flight value of 0.165 (Figure 11B). Noise levels were slightly smaller between the peaks between locations 48 and 96 in the 10.49 µm band (Figure 11B). The 12.09 µm band in the 271.4 K scene had noise levels between 0.48 K and 0.60 K in pixels 32, 40, 48, 56, 64, 72, 80, 88, 96, 104, and 112, which are between 5 and 32 percent higher than the interpolated pre-flight value of 0.455 (Figure 11C). The 12.09 µm noise levels in the 271.4 K scene, between the peaks in pixels 32–104, were between 8 and 17% below the preflight value, ranging from 0.38 K to 0.42 K (Figure 11C).

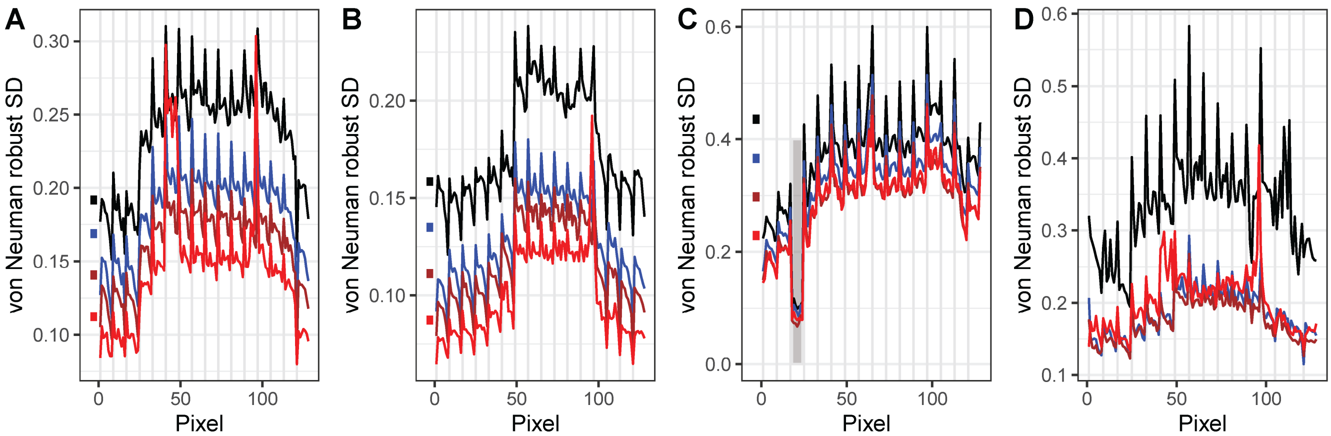

Figure 11. The robust standard deviation of band brightness temperature and retrieved skin temperature measured by cross-track successive differences vs. pixel position in the focal plane array: (**A**) 8.78 µm; (**B**) 10.49 µm; (**C**) 12.09 µm; (**D**) retrieved skin temperature. Lines are from scenes with different mean ocean temperatures (red: 301.8 K; brown: 291 K; blue: 279.7 K; black 271.4 K). Colored squares to the left of zero are interpolated from pre-flight measurements of NEdT in the laboratory [44]. The gray area in (**C**) is a region of non-responsive pixels interpolated from data in the other two wavelength bands. Noise levels in retrieved skin temperatures (**D**) are affected by noise in the individual wavelength bands.

There were similar patterns in the scenes with higher temperatures (Figure 11). Noise levels in the retrieved skin temperatures (LST, Figure 11D) are dependent upon those in the individual wavelength bands, but the specific numerical relationship depends upon the TES temperature retrieval algorithm. As in the wavelength bands, retrieved skin temperature noise is greater in the middle of the focal plane than on the edges, and there is an eight-pixel periodicity in the noise peaks (Figure 11D). There is little dependence of retrieved skin temperature noise upon scene temperature, except at the lowest scene temperature (271.4 K).

The focal plane array is arranged in 4 × 256-pixel blocks for each wavelength, with the long axis in the along-track direction. The four pixels in each row are combined by time-delayed integration (TDI), yielding a 1 × 256 pixel column. In the L1A to L1B processing, adjacent pairs of pixels in each column are combined, yielding a 1 × 128-pixel cross-track observation set. The readout circuit for the focal plane array used a 32-channel analog multiplexer [50]. The 8-pixel periodicity in noise levels in each of the channels is likely the result of a noise spike when the multiplexer index resets to zero after reading each group of 32 pixels in the columns of the 4 × 256-pixel blocks. This would lead to a noise spike every 16 pixels in the L1A datasets after TDI and to a noise spike every 8 pixels in the L1B data, as seen in Figure 11.

3.6. Focal Plane Non-Uniformity (Spatial Noise)

There are pixel-to-pixel differences in sensitivity across the FPA, as evident in the variation in the black body digital numbers (Figure 12). The patterns differ among bands because different parts of the FPA are used to capture data from different wavelength bands. The differences between individual pixels and the smoothed lines likely come from variations in the electrical and optical characteristics of individual pixels in the FPA. There is a quasi-parabolic relationship between pixel number and digital number in the 8.78 µm band (Figure 12A) and a quasi-linear increasing relationship in the 10.49 µm band (Figure 12B); in the 12.09 µm band, there is a nonlinear relationship with a shape change around pixel 64 (Figure 12C).

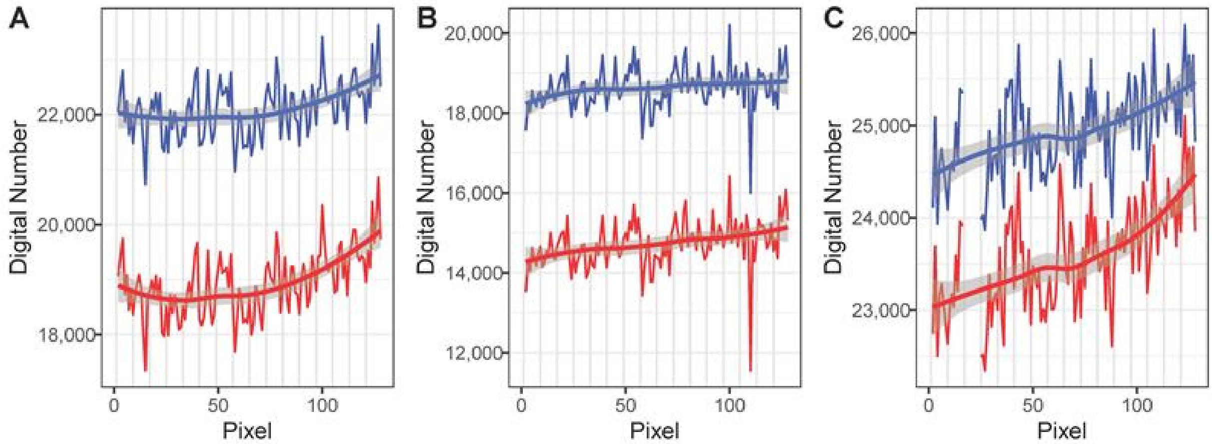

Figure 12. Focal plane non-uniformity in black body counts in the 8.48 µm (**A**), 10.49 µm (**B**), and 12.09 µm (**C**) bands. Thin lines are mean values (blue = 293 K black body; red = 319 K black body). Missing data in panel (**C**) are due to non-functional pixels in the region 18–24 that were damaged during pre-flight testing. Smoothed lines and shaded regions are loess regressions and 95% confidence limits, respectively. Pixel 1 data were removed for clarity. Vertical grey lines are at 8-pixel intervals. Data are from scene 2 (Table 1).

Table 1. Black body thermistor temperature variation in English Channel scenes. Temperature means and standard deviations are from 5 platinum resistance thermometers embedded in the center and perimeter of each black body.

Scene Number	Orbit_Scene	Date Time (UTC)	Cold BB		Hot BB	
			Mean (K)	sd	Mean (K)	sd
1	10043_007	13 April 2020 14:24:40	292.800	0.170	318.905	0.144
2	10072_005	15 April 2020 11:13:12	293.015	0.172	318.907	0.149
3	10392_001	6 May 2020 02:37:16	294.086	0.178	318.918	0.145
4	16665_003	14 June 2021 10:53:10	293.195	0.172	318.919	0.145
5	17169_005	16 July 2021 21:47:31	292.624	0.171	318.905	0.150
6	17615_009	14 August 2021 13:27:20	292.868	0.169	318.912	0.143
7	17983_010	7 September 2021 04:16:44	293.848	0.175	318.907	0.145

The elevations of the lines on the digital number axis differ among scenes, but the deviations of pixels from the smoothed lines are nearly identical among all scenes in each wavelength band independent of black body temperature. Scene 5 warm black body digital numbers are approximately 1000 counts higher than those from the other scenes, indicating that the blackbody was colder than in the other scenes; however, the warm black body PRT temperatures in scene 5 differ by less than 10 mK from those in the other scenes (Table 1), so the difference must be due to something else, perhaps instrument component temperatures that are different from the other scenes. Future analysis of engineering data may resolve this discrepancy.

Ocean scene brightness temperatures also show consistent patterns of variation among pixels in the FPA. In nine scenes from the English Channel, retrieved between February 2019 and September 2021, there were clear signs of consistently low-sensitivity pixels and high-sensitivity pixels (Figure 13). There were also cross-array variations in sensitivity, with pixels 100–128 having lower sensitivity at all three wavelengths, the effect being most evident in the 12.09 µm wavelength band. In the 8.78 µm band, the median anomaly in pixels 100–128 decreased from −0.04 to −0.12 K (slope = −0.0046, R^2 = 0.737, N = 29, RMSE = 0.0236 K, $p < 0.001$). In the 10.49 µm band, the median anomaly in pixels 100–128 decreased from −0.003 to −0.19 K (slope = −0.0043, R^2 = 0.142, N = 29, RMSE = 0.0910 K, $p < 0.05$). In the 12.09 µm band, the median anomaly in pixels 100–128 decreased from −0.001 to −0.437 (slope = −0.0174, R^2 = 0.744, N = 29, RMSE = 0.0886 K, $p < 0.001$). The broad patterns differed among wavelengths, as did the locations of the especially high and low-sensitivity pixels. Brightness temperature anomalies varied in magnitude but were consistently found in the same pixels within a band. In the 8.48 µm band, anomalies as low as −0.45 K were observed in pixels 6, 61, and 93. Negative anomalies lower than −1.4 K were observed in pixel 1, and anomalies lower than −2.5 K were observed in pixels 110–111 in the 10.49 µm band. Negative anomalies lower than −0.5 K in pixels 11, 12, 91, 92, 117, 118, and 123–128 exceeded −1.0 K in pixel 92 in the 12.09 µm band. The primary consistent patterns across wavelengths were (1) a tendency for anomalies at 8-pixel intervals along the FPA (Figure 13), which probably derives from small transients caused by the 32-channel multiplexer, as described in the section on noise (3.5), and (2) a fall-off in sensitivity in pixels 100–128.

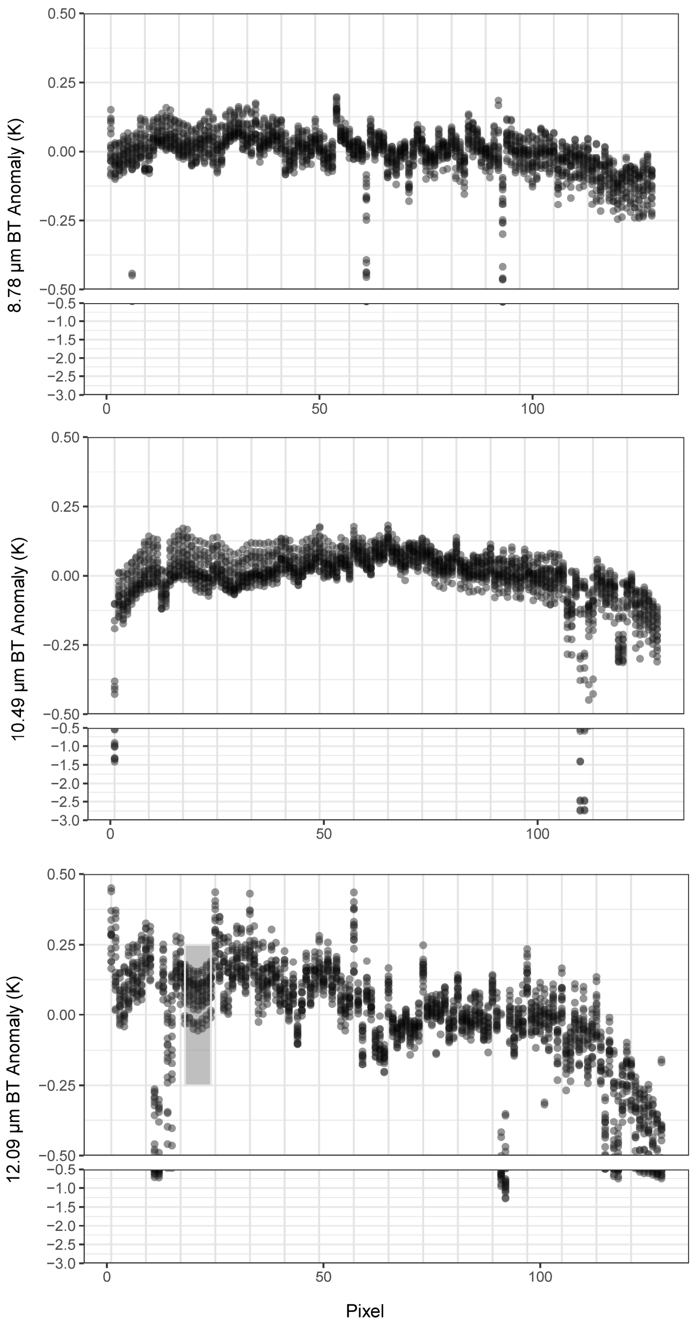

Figure 13. Mean brightness temperature anomalies within the focal plane array in 9 scenes retrieved between February 2019 and September 2021. Dots are median anomalies in single scenes. The gray area in the 12.09 µm graph is a region of non-responsive pixels interpolated from data in the other two wavelength bands. Vertical lines are at 8-pixel intervals.

3.7. Black Body Performance

Black body data from seven scenes of the English Channel (longitude 0) were analyzed (Table 1). Each black body has five embedded platinum resistance thermometers (PRT), which are measured 52 times during each scene retrieval of 44 mirror scans. Four PRTs are arranged around the perimeter of each black body, and the fifth is in the center [53]. The PRT temperatures in the black bodies vary among each other by up to 0.4 to 0.6 K during retrieval of individual scenes, but the rank order of the temperatures differs between the hot and cold BBs (Figure 14). The cold black body temperature was highest when the space station was on the dark side of the earth (UTC times 02:37 and 04:16) and lowest just after the ISS passed into the earth's shadow (UTC 21:47) (Table 1). The cold black body had a larger temperature gradient (0.483 K) than the warm black body (0.436 K), based on the mean temperature difference between the warmest and coolest PRTs (Figure 14). The PRT temperature rank orders differed between the cold and hot black bodies, suggesting that there is also a difference in the geometry of the temperature gradients across the black bodies. The individual PRTs in the warm black body have smaller overall temperature variations among each other (Table 1) but larger within-scene temperature transients than the thermistors in the cold black body (Figure 14).

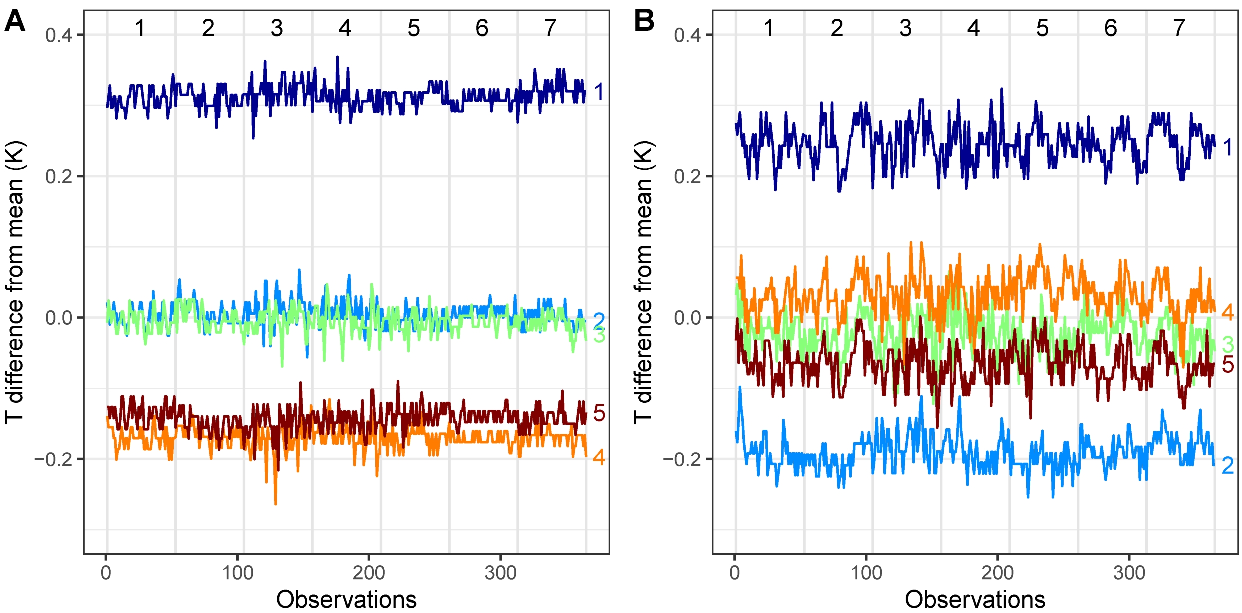

Figure 14. Blackbody PRT temperature anomalies relative to temperature mean during 7 scenes listed in Table 1: (**A**) cold black body; (**B**) hot black body. Scene numbers (Table 1) are at the top of each panel. Line colors identify individual PRTs. PRT numbers are on the right-hand side of each panel.

The temperature gradients in both black bodies were stable despite the 1.5 K changes in temperature of the cold black body between the sun and shade portions of the orbit (Table 1, Figure 14). These temperature gradients and variations contribute to the overall uncertainty of the radiometric calibration.

4. Discussion

4.1. Biases

ECOSTRESS Collection 1 has a median skin temperature cold bias of −1.05 K relative to in situ observations with an RMS error of 0.57 K (Figure 2A). Bulk–skin temperature differences [2,34,64] cannot account for the bias relative to in situ observations because the bias has an asymptote of approximately −1 K at wind speeds over 10 ms^{-1} (Figure 3). The RMS error relative to in situ is approximately 1.6× greater than the RMS error of AVHRR relative to in situ and 2.3× greater than the RMS error of VIIRS and MODIS relative to in situ. The SST retrieval bias derives in part from median brightness temperature biases of

−1.74, −1.45, and −1.77 K in the three active wavelength bands (Figure 5). These biases are not completely corrected in Collection 2 (Figure 5). The radiance calibration is dependent upon measurements of two onboard black bodies, each of which has five embedded platinum resistance thermometers. Preflight validation with an external calibration target indicated no relationship between brightness temperature bias and NIST-traceable external target temperature; RMSE was 36.2, 46.8, and 44.6 mK at 8.78, 10.49, and 12.09 µm, respectively [51].

Most SSTs in the iQuam dataset are below 20 °C, the temperature of the ECOSTRESS cold black body (~20 to 25 °C), so the linear calibration of the sensor radiances relative to the black bodies could lead to errors at temperatures below 22 °C [40,41] (e.g., Mittaz et al. 2009; Mittaz and Harris 2011), although there is little evidence of temperature dependence of the bias in the post-flight data (Figure 2) or in the pre-flight data. There is only very weak evidence of nonlinearity in the instrument response (Figure 6). The temperature biases were stable over the period 2019–2022 (Figure 10).

Retrieved emissivities over the ocean are generally below the range of physical possibility (Figure 7), and the uncertainty statistics derived from the TES algorithm do not accurately estimate the true biases (Figure 8). The overall effect of the emissivity biases partially compensates for the cold biases in the brightness temperatures (Figure 9), so the retrieved temperatures are not as low as would be expected from the brightness temperature biases.

4.2. Radiometric Noise (Temporal and Spatial Noise)

Temporal, radiometric noise (cross-track) varies as a function of scene temperature and detector in the focal plane array (Figure 11) and propagates from the individual wavelength band radiances and brightness temperatures to the retrieved skin temperature. The lowest radiometric noise was in scenes with the highest temperature and vice versa. Noise levels in detectors at both ends of the focal plane were similar to pre-flight values, but the middle of the focal plane had noise levels approximately 2× greater. There was also a spike in noise at eight detector intervals along the focal plane array. We suspect that the spikes are caused by the 32-channel multiplexor in the readout circuit.

Spatial radiometric noise (focal plane non-uniformity) is evident from clear detector-to-detector variations in the sensitivity of the ECOSTRESS focal plane (Figures 12 and 13), with pixels at one end having lower sensitivity than those at the other end. The origin of the non-uniformity is unknown; however, there are several possibilities. One possibility is that there are differences in spectral response among detectors, which could lead to non-uniformities because the radiometric calibration of ECOSTRESS uses a single lookup table for each wavelength band to relate detector digital numbers to radiance [50]. Focal plane non-uniformities in VIIRS SNPP are at least partially due to differences in spectral response among detectors [94,95]. In VIIRS JPSS1, the non-uniformities increase with source temperature [96], which could also be related to differences in spectral response. These detector-to-detector differences in the spectral response of VIIRS lead to detector-to-detector variations in retrieved temperature of up to 7 mK [97]. By comparison, the detector-to-detector differences in ECOSTRESS brightness temperatures are up to 375 mK in the 8.78 and 10.49 µm bands and up to 875 mK in the 12.09 µm band (Figure 13). These are so large that detector-to-detector differences in spectral response are unlikely to be responsible.

A second possibility is that the geometry of the optical system leads to a fall-off in incident radiation at the two ends of the focal plane array. A ray-tracing figure of the optical system [98] indicates that the angle of incidence of radiation differs from approximately 10° at one end of the focal plane to 45° at the other end, which would cause a gradient in detector response. However, a full evaluation of the optical model of the telescope and focal plane will be necessary to determine the magnitude of this effect.

Focal plane non-uniformity leads to along-track striping in all bands. After reprojecting the swath data onto a rectilinear geographic coordinate system, the non-uniformity also leads to a checkerboard artifact because geographically adjacent pixels may come from opposite ends of the focal plane due to the 15–30 pixel overlap of adjacent mirror swaths [52], and one end of the focal plane has a negative temperature bias relative to the other end (Figure 13).

Spatial and temporal radiometric noise in ECOSTRESS is greater than in other satellite instruments used for operational SST retrievals (VIIRS [49,95,99], SLSTR [100], MODIS [101,102], Table 2) but is similar to the expected radiometric noise in future high-resolution missions (TRISHNA [103], SBG [104], LSTM [105]) (Table 2). The high temporal (cross-track) radiometric noise level of ECOSTRESS derives from the short integration times required for retrieving data at a 70 m spatial scale with a push-whisk instrument. The spatial noise is a result of non-uniformities along the focal plane.

Table 2. Radiometric noise at 300 K of satellite instruments used in operational SST retrievals and future planned high-resolution missions. Values are noise-equivalent delta temperatures in mK. Wavelength bands are not identical in the different instruments. * SBG and LSTM values are predictions; the remainder are measured temporal noise values.

Instrument	8.5 µm		10–11 µm		12 µm	
Noise Type	Spatial	Temporal	Spatial	Temporal	Spatial	Temporal
VIIRS		55	25	23	30	39
SLSTR			3	13	3	15
MODIS	600	30	26	30	32	40
ECOSTRESS	375	100–300	375	60–180	625	180–520
TRISHNA	95	80	70	70	60	70
SBG *		100		100		100
LSTM *		100		100		100

4.3. Black Body Performance

One possible source of brightness temperature biases in the individual wavelength bands is in the black bodies themselves. Variability among ECOSTRESS thermistors is approximately 10× greater than in other satellite instruments used for SST retrievals: ATSR [106], SLSTR [45,100], MODIS [107], and VIIRS [99] (Figure 14, Tables 1 and 3). This high variability means that the uncertainty in the black body temperatures is large, and this uncertainty propagates through the radiance calibration process to uncertainty in the temperature retrievals. Platinum thermistors can differ from the standard resistance versus temperature relationship by as much as 0.5 K after encapsulation into black body assemblies as a result of straining of the platinum wire during manufacturing and testing, leading to biases [108]. Depending upon which subset of thermistors is used to determine black body temperature, biases in radiance calibration can arise. This is a greater problem for ECOSTRESS than for the other instruments because of the high variability among thermistor temperatures.

Table 3. Variation among thermistor temperatures in black bodies of satellite instruments used for SST retrievals. Values are standard deviations in mK.

Instrument	Hot BB sd (mK)	Cold BB sd (mK)	Source
ATSR	6.2	5.02	62
SLSTR-A	11.6	9	60
SLSTR-B	27	8	63
MODIS-A	30	7	64
VIIRS-SNPP		4	59
VIIRS-N20		8	59
ECOSTRESS	146	172	Table 1

4.4. Radiometric Uncertainty

A full radiometric uncertainty analysis [100] is beyond the scope of this paper, but several contributions to uncertainty in the radiance retrievals from ECOSTRESS can be identified. Detector temporal and spatial noise (NEdT) varies as a function of scene temperature, detector, and wavelength band (Figure 11). Black body temperature uncertainty derives from the variation among thermistors embedded in the black bodies (Figure 14, Table 1), and since the black body temperatures are used in the radiance calibration, their uncertainty contributes to uncertainty in retrieved radiances. Focal plane non-uniformities that are not corrected by the calibration algorithm (Figure 13) cause uncertainties in radiance retrievals on a pixel-to-pixel basis in earth scenes. The total uncertainty in Table 4 is the linear sum of all contributions.

Table 4. Sources of uncertainty in ECOSTRESS radiance retrievals for an earth scene at 280 K. Values are in mK. For details of quantities, see Appendix A.

Source of Uncertainty	Uncertainty Estimation	8.78 μm	10.49 μm	12.09 μm
NEdT	Figure 11	120–250	60–180	180–520
Cold BB PRT temperatures	$\frac{\partial L_E}{\partial L_{BB}} * \frac{\partial L_{BB}}{\partial T_{BB}}\vert_{T_{BB}} * \frac{\partial T_{BB}}{\partial T_{PRT}} * \frac{\partial T_E}{\partial L_E}\vert_{T_E} * \Delta PRT$	10	9.6	9.4
Hot BB PRT temperatures		11.4	10.2	9.6
Focal Plane Non-uniformity	Figure 14	125	250	750
Total		266–396	330–450	949–1289

The uncertainties in Table 4 are much larger than those reported for SLSTR [100], but they are generally within the required specifications of the ECOSTRESS instrument for land surface temperature acquisitions (uncertainty < 1 K in retrievals from a 300 K earth scene) [20]. These results highlight the differences in requirements of SST missions compared to LST missions. Because surface properties of the ocean are so much more tightly constrained than those of land, the expectation for SST missions (SST retrieval uncertainty < 0.3 K and top of atmosphere brightness temperature uncertainty < 0.2 K [100]) is much more stringent than for LST missions. On land, surface emissivity is unknown a priori, so temperature retrievals necessitate simultaneous emissivity retrievals and the solving of N equations for N + 1 unknowns, all of which increase the uncertainty of the retrievals. Therefore, land surface missions have less stringent uncertainty requirements than SST missions. The next three high spatial resolution thermal missions (TRISHNA, SBG, LSTM) have been designed primarily for land surface temperature retrieval and will have lower performance on SST retrieval but much higher spatial resolution than current SST missions. Table 4 indicates that retrieval of high-quality SST products from ECOSTRESS and those future missions will require careful attention to noise and uncertainty reduction in the retrieval algorithms.

5. Conclusions

ECOSTRESS serves as a precursor for future planned 50–60 m scale thermal missions TRISHNA (CNES-ISRO) [56], SBG (NASA) [57], and LSTM (ESA) [58], which together are expected to provide global daily 50–60 m coverage of the ocean within 100 km of the world's coasts. Lessons learned from ECOSTRESS will be extremely valuable in planning for future missions.

The ECOSTRESS Collection 1 Level-2 surface temperature product (2018–present) has a ~1 °K cold bias relative to VIIRS observations [23] and to in situ observations on lakes [20,21], coastal waters [22], and the ocean (Figure 2). The RMSE of the surface temperature product relative to in situ was 0.57 K, somewhat larger than the RMSE for MODIS and VIIRS (0.25 K) and AVHRR (0.39 K) operational products [92]. The brightness temperatures have a cold bias relative to RTTOV radiance transfer simulations (Figures 5 and 6). Ocean surface emissivities retrieved with the ECOSTRESS temperature emissivity separation algorithm are much lower than either laboratory measurements or RTTOV simulations

(Figure 7). The instrument has some calibration drift, evidenced by the 0.1 K/year negative trend in model-observation double differences with respect to GOES-ABI in the 10 and 12 µm channel brightness temeratures over the period 2019–2022 (Figure 10). Temporal (cross-track) radiometric noise is temperature dependent and is higher than expected from pre-flight measurements (Figure 11), and is much larger than temporal radiometric noise of operational instruments used for SST retrievals (ATSR, SLSTR, MODIS, VIIRS, Table 2). The onboard blackbody temperature gradients are much larger than gradients on other operational sensors (Tables 1 and 3). Detector to detector differences in brightness temperatures are up to 375 mK in the 8.78 and 10.49 µm bands and up to 875 mK in the 12.09 µm band (Figure 13), leading to checkerboard artefacts when overlapping pixels are reprojected onto a geographic coordinate system. For the creation of a sea surface temperature product that meets the requirements of the SST community, it will be necessary to develop calibration methods that reduce the brightness temperature biases and reduce the detector to detector differences in sensitivity.

The high spatial resolution of ECOSTRESS and the future TRISHNA, SBG, and LSTM instruments are potential game-changers for oceanography because their small pixel sizes permit resolution of submesoscale features on spatial scales of 2× pixel size (100 to 200 m), far smaller than what is detectable by current operational SST instruments. However, the spatial and temporal radiometric noise levels of ECOSTRESS and the planned instruments are higher than in current operational SST instruments, requiring the development of new techniques for noise reduction to enable the detection of filaments, fronts, and gradients in order to take advantage of the higher spatial resolution. ECOSTRESS can provide a test bed for the necessary algorithm development.

Author Contributions: Conceptualization, D.S.W., N.W. and S.A.W.; methodology, D.S.W. and N.W.; software, D.S.W.; validation, D.S.W. and N.W.; formal analysis, D.S.W.; data curation, D.S.W.; writing—original draft preparation, D.S.W.; writing—review and editing, D.S.W., S.A.W., N.W. and J.V.-C.; visualization, D.S.W.; project administration, D.S.W.; funding acquisition, D.S.W., S.A.W. and J.V.-C. All authors have read and agreed to the published version of the manuscript.

Funding: This research was funded by NASA grants 80NSSC20K0074 and 80NSSC23K0643. J.V.-C. was supported at the Jet Propulsion Laboratory, California Institute of Technology, under a contract with the National Aeronautics and Space Administration (80NM0018D0004).

Data Availability Statement: ECOSTRESS Collection 1 Level 1B and Level 2 files are available at https://e4ftl01.cr.usgs.gov (accessed on 22 May 2024) and can be searched via https://search.earthdata.nasa.gov (accessed on 22 May 2024). Level 1A instrument data and calibration files are available by request from the ECOSTRESS instrument team at the NASA Jet Propulsion Laboratory.

Acknowledgments: Data from GOES-16, GOES-17, Himawari-8, MSG-1, MSG-3, and MSG-4 were provided by the Group for High-Resolution Sea Surface Temperature (GHRSST) and the National Oceanic and Atmospheric Administration (NOAA) and were obtained from the GHRSST archive at the NASA Physical Oceanography Distributed Active Archive Center (PODAAC: https://podaac.jpl.nasa.gov, accessed on 22 May 2024). ECMWF ERA-5 data were obtained from the Research Data Archive at the US National Center for Atmospheric Research (https://rda.ucar.edu, accessed on 22 May 2024). NOAA iQuam data were obtained from https://www.star.nesdis.noaa.gov/socd/sst/iquam/data.html (accessed on 22 May 2024). We thank Kerry Cawse-Nicholson (NASA JPL) for access to ECOSTRESS L1A black body calibration files and raw pixel data files. We thank three anonymous reviewers for their helpful comments on the manuscript.

Conflicts of Interest: The authors declare no conflicts of interest.

Appendix A

We follow Smith et al. [100] in developing a partial uncertainty budget from the data presented above. Partial derivatives were calculated using Maple 15 [109]. The radiance calibration equation for ECOSTRESS takes the form

$$L_E = a_0 + a_1 D_E \tag{A1}$$

where L_E is the radiance of the earth scene, and D_E is the digitizer counts from the earth scene. The gain (a_1) and offset (a_0) are calculated from the blackbody scans:

$$a_0 = \frac{D_c L_h - D_h L_c}{D_c - D_h} \tag{A2}$$

$$a_1 = \frac{L_c - L_h}{D_c - D_h} \tag{A3}$$

where D_c and D_h are the digitizer counts from the cold and hot black bodies, and L_c and L_h are the radiances predicted from the temperatures of the thermistors embedded in the cold and hot black bodies. Radiances were calculated using the Planck equation:

$$L(\lambda, T) = \frac{2hc^2}{\lambda^5 \left(\exp\left(\frac{hc}{\lambda kT}\right) - 1\right)} \tag{A4}$$

where λ is the wavelength in m, T is the temperature, h (Planck's constant) = 6.62607015 $\times$ 10^{-34} J s, c (speed of light) = 299,792,458 m s^{-1}, and k (Boltzmann's constant) = 1.380649 $\times$ 10^{-23} J K^{-1}. To scale L in units of W m^{-2} sr^{-1} µm^{-1}, the result is divided by 10^6.

The uncertainties in scene radiance associated with the digitizer count variations are related to the partial derivatives of scene radiance with respect to scene digitizer counts (Equation (A5)), black body digitizer counts (Equations (A6) and (A7)), and black body radiances (Equations (A8) and (A9))

$$\frac{\partial L_E}{\partial D_E} = a1 \tag{A5}$$

$$\frac{\partial L_E}{\partial D_c} = a1 \frac{\overline{D_c} - D_E}{\overline{D_c} - \overline{D_h}} \tag{A6}$$

$$\frac{\partial L_E}{\partial D_h} = a1 \frac{D_E - \overline{D_c}}{\overline{D_c} - \overline{D_h}} \tag{A7}$$

$$\frac{\partial L_E}{\partial L_c} = \frac{D_E - \overline{D_c}}{\overline{D_c} - \overline{D_h}} \tag{A8}$$

$$\frac{\partial L_E}{\partial L_h} = \frac{\overline{D_c} - D_E}{\overline{D_c} - \overline{D_h}} \tag{A9}$$

where the overbar symbols represent means, either of the scene or the detector, and coefficient $a1$ is defined in Equation (A3).

The uncertainty in radiance associated with a scene or black body temperature variation is related to the partial derivative of the Planck equation (Equation (A4)), evaluated at λ = central wavelength and T = temperature.

$$\frac{\partial L}{\partial T} = \frac{\varepsilon 2h^2 c^3 \exp\left(\frac{hc}{\lambda \mathrm{kT}}\right)}{\lambda^6 k T^2 \left(\exp\left(\frac{hc}{\lambda \mathrm{kT}}\right) - 1\right)^2} \tag{A10}$$

The uncertainty in retrieved radiance due to variation in the black body thermistors (ΔPRT) is estimated with Equation (A11)

$$\frac{\partial L_E}{\partial T_{PRT}} = \frac{\partial L_E}{\partial L_{BB}} \frac{\partial L_{BB}}{\partial T_{BB}} |_{T_{BB}} \frac{\partial T_{BB}}{\partial T_{PRT}} \Delta PRT \tag{A11}$$

using Equations (A8) and (A9), with Equation (A10) evaluated at the band wavelength and the black body temperature, where the partial derivative of black body temperature with respect to PRT temperature is 1/5 (because there are 5 PRTs per black body) and ΔPRT is the standard deviation of PRT temperatures (Table 1).

The uncertainty in retrieved earth temperature is obtained using Equation (A11), with Equation (A10) evaluated at the average scene temperature T_E.

$$\frac{\partial T_E}{\partial T_{PRT}} = \frac{\partial L_E}{\partial T_{PRT}} \left(\frac{\partial L_E}{\partial T_E} |_{T_E} \right)^{-1} \tag{A12}$$

References

1. Ohring, G.; Wielicki, B.; Spencer, R.; Emery, B.; Datla, R. Satellite Instrument Calibration For Measuring Global Climate Change—Workshop Report. *Bull. Am. Meteorol. Soc.* **2005**, *86*, 1303–1314. [CrossRef]
2. Minnett, P.J.; Alvera-Azcárate, A.; Chin, T.M.; Corlett, G.K.; Gentemann, C.L.; Karagali, I.; Li, X.; Marsouin, A.; Marullo, S.; Maturi, E.; et al. Half a Century of Satellite Remote Sensing of Sea-Surface Temperature. *Remote Sens. Environ.* **2019**, *233*, 111366. [CrossRef]
3. O'Carroll, A.G.; Armstrong, E.M.; Beggs, H.M.; Bouali, M.; Casey, K.S.; Corlett, G.K.; Dash, P.; Donlon, C.J.; Gentemann, C.L.; Høyer, J.L.; et al. Observational Needs of Sea Surface Temperature. *Front. Mar. Sci.* **2019**, *6*, 420. [CrossRef]
4. Merchant, C.J.; Embury, O.; Bulgin, C.E.; Block, T.; Corlett, G.K.; Fiedler, E.; Good, S.A.; Mittaz, J.; Rayner, N.A.; Berry, D.; et al. Satellite-Based Time-Series of Sea-Surface Temperature since 1981 for Climate Applications. *Sci. Data* **2019**, *6*, 223. [CrossRef] [PubMed]
5. Dash, P.; Ignatov, A.; Kihai, Y.; Sapper, J. The SST Quality Monitor (SQUAM). *J. Atmos. Ocean. Technol.* **2010**, *27*, 1899–1917. [CrossRef]
6. Hook, S.; Smyth, M.; Logan, T.; Johnson, W. ECOSTRESS Geolocation Daily L1B Global 70 m V001 [Data Set]. Available online: https://doi.org/10.5067/ECOSTRESS/ECO1BGEO.001 (accessed on 17 March 2024).
7. Hook, S.; Smyth, M.; Logan, T.; Johnson, W. ECOSTRESS At-Sensor Calibrated Radiance Daily L1B Global 70 m V001. Available online: https://doi.org/10.5067/ECOSTRESS/ECO1BRAD.001 (accessed on 17 March 2024).
8. Hook, S.; Hulley, G. ECOSTRESS Land Surface Temperature and Emissivity Daily L2 Global 70 m V001. Available online: https://doi.org/10.5067/ECOSTRESS/ECO2LSTE.001 (accessed on 23 March 2024).
9. Hook, S.; Hulley, G. ECOSTRESS Cloud Mask Daily L2 Global 70 m V001. Available online: https://doi.org/10.5067/ECOSTRESS/ECO2CLD.001 (accessed on 17 March 2024).
10. Hulley, G.C.; Hook, S.J. *ECOSTRESS Level-2 Land Surface Temperature and Emissivity Algorithm Theoretical Basis Document (ATBD)*; Jet Propulsion Laboratory: Pasadena, CA, USA, 2016. Available online: https://lpdaac.usgs.gov/documents/1324/ECO2_LSTE_ATBD_V1.pdf (accessed on 22 May 2024).
11. Gillespie, A.; Rokugawa, S.; Matsunaga, T.; Cothern, J.S.; Hook, S.; Kahle, A.B. A Temperature and Emissivity Separation Algorithm for Advanced Spaceborne Thermal Emission and Reflection Radiometer (ASTER) Images. *IEEE Trans. Geosci. Remote Sens.* **1998**, *36*, 1113–1126. [CrossRef]
12. Petrenko, B.; Ignatov, A.; Kihai, Y.; Stroup, J.; Dash, P. Evaluation and Selection of SST Regression Algorithms for JPSS VIIRS. *JGR Atmos.* **2014**, *119*, 4580–4599. [CrossRef]
13. Merchant, C.J.; Harris, A.R.; Maturi, E.; Embury, O.; MacCallum, S.N.; Mittaz, J.; Old, C.P. Sea Surface Temperature Estimation from the Geostationary Operational Environmental Satellite-12 (GOES-12). *J. Atmos. Ocean. Technol.* **2009**, *26*, 570–581. [CrossRef]
14. Watts, P.D.; Allen, M.R.; Nightingale, T.J. Wind Speed Effects on Sea Surface Emission and Reflection for the Along Track Scanning Radiometer. *J. Atmos. Ocean. Technol.* **1996**, *13*, 126–141. [CrossRef]
15. Masuda, K. Infrared Sea Surface Emissivity Including Multiple Reflection Effect for Isotropic Gaussian Slope Distribution Model. *Remote Sens. Environ.* **2006**, *103*, 488–496. [CrossRef]
16. Newman, S.M.; Smith, J.A.; Glew, M.D.; Rogers, S.M.; Taylor, J.P. Temperature and Salinity Dependence of Sea Surface Emissivity in the Thermal Infrared. *Q. J. R. Meteorol. Soc.* **2005**, *131*, 2539–2557. [CrossRef]
17. Hocking, J.; Rayer, P.; Rundle, D.; Saunders, R.; Matricardi, M.; Geer, A.; Brunel, P.; Vidot, J. *RTTOV V12 Users Guide*; Eumetsat NWP SAF: Reading, UK, 2019; Available online: https://nwp-saf.eumetsat.int/site/download/documentation/rtm/docs_rttov12/users_guide_rttov12_v1.3.pdf (accessed on 22 May 2024).
18. Gladkova, I.; Ignatov, A.; Semenov, A. Analaysis of ABI Bands and Regressors in the ACSPO GEO NLSST Algorithm. In Proceedings of the SPIE Defense + Commercial Sensing, Orlando, FL, USA, 3–7 April 2022; SPIE: Bellingham, WA, USA, 2022; Volume 12118, p. 1211804. [CrossRef]
19. Saux Picart, S. *Algorithms Theoretical Basis Document for Low Earth Orbiter Sea Surface Temperature Processing*; Eumetsat OSI SAF: Lannion, France, 2018; Available online: https://osi-saf.eumetsat.int/lml/doc/osisaf_cdop2_ss1_atbd_leo_sst.pdf (accessed on 22 May 2024).
20. Hook, S.J.; Cawse-Nicholson, K.; Barsi, J.; Radocinski, R.; Hulley, G.C.; Johnson, W.R.; Rivera, G.; Markham, B. In-Flight Validation of the ECOSTRESS, Landsats 7 and 8 Thermal Infrared Spectral Channels Using the Lake Tahoe CA/NV and Salton Sea CA Automated Validation Sites. *IEEE Trans. Geosci. Remote Sens.* **2020**, *58*, 1294–1302. [CrossRef]

21. Hulley, G.C.; Gottsche, F.M.; Rivera, G.; Hook, S.J.; Freepartner, R.J.; Martin, M.A.; Cawse-Nicholson, K.; Johnson, W.R. Validation and Quality Assessment of the ECOSTRESS Level-2 Land Surface Temperature and Emissivity Product. *IEEE Trans. Geosci. Remote Sens.* **2022**, *60*, 1–23. [CrossRef]
22. Shi, J.; Hu, C. Evaluation of ECOSTRESS Thermal Data over South Florida Estuaries. *Sensors* **2021**, *21*, 4341. [CrossRef] [PubMed]
23. Weidberg, N.; Wethey, D.S.; Woodin, S.A. Global Intercomparison of Hyper-Resolution ECOSTRESS Coastal Sea Surface Temperature Measurements from the Space Station with VIIRS-N20. *Remote Sens.* **2021**, *13*, 5021. [CrossRef]
24. Xu, F.; Ignatov, A. In Situ SST Quality Monitor (iQuam). *J. Atmos. Ocean. Technol.* **2014**, *31*, 164–180. [CrossRef]
25. NOAA/NESDIS/STAR GHRSST L2P ACSPO America Region SST from GOES-16 ABI. Available online: https://doi.org/10.5067/GHG16-2PO27 (accessed on 23 March 2024).
26. NOAA/NESDIS/STAR GHRSST L2P ACSPO America Region SST from GOES-17 ABI. Available online: https://doi.org/10.5067/GHG17-2PO71 (accessed on 23 March 2024).
27. NOAA/NESDIS/STAR GHRSST NOAA/STAR Himawari-08 AHI L2P Pacific Ocean Region SST v2.70 Dataset in GDS2. Available online: https://doi.org/10.5067/GHH08-2PO27 (accessed on 23 March 2024).
28. NOAA/NESDIS/OSPO GHRSST Level 2P Indian Ocean Regional Skin Sea Surface Temperature v1.0 from the Spinning Enhanced Visible and InfraRed Imager (SEVIRI) on the Meteosat Second Generation-1 (MSG-1) Satellite. Available online: https://doi.org/10.5067/GHMG1-2PO01 (accessed on 17 March 2024).
29. NOAA/NESDIS/OSPO NOAA GHRSST Level 2P Indian Ocean Regional Skin Sea Surface Temperature v1.0 from the Spinning Enhanced Visible and InfraRed Imager (SEVIRI) on the Meteosat Second Generation-2 (MSG-2) Satellite. Available online: https://doi.org/10.5067/GHMG2-2PO10 (accessed on 17 March 2024).
30. NOAA/NESDIS/OSPO NOAA GHRSST Level 2P Atlantic Ocean Regional Skin Sea Surface Temperature v1.0 from the Spinning Enhanced Visible and InfraRed Imager (SEVIRI) on the Meteosat Second Generation-4 (MSG-4) Satellite. Available online: https://doi.org/10.5067/GHMG4-2PO01 (accessed on 23 March 2024).
31. Masuda, K.; Takashima, T.; Takayama, Y. Emissivity of Pure and Sea Waters for the Model Sea Surface in the Infrared Window Regions. *Remote Sens. Environ.* **1988**, *24*, 313–329. [CrossRef]
32. Masuda, K. Dependence of Sea Surface Emissivity on Temperature-dependent Refractive Index. *Q. J. R. Meteorol. Soc.* **2008**, *134*, 541–545. [CrossRef]
33. NOAA/NESDIS/OSPO NOAA GHRSST Level 2P Atlantic Ocean Regional Skin Sea Surface Temperature v1.0 from the Spinning Enhanced Visible and InfraRed Imager (SEVIRI) on the Meteosat Second Generation-3 (MSG-3) Satellite. Available online: https://doi.org/10.5067/GHMG3-2PO02 (accessed on 23 March 2024).
34. Minnett, P.J.; Smith, M.; Ward, B. Measurements of the Oceanic Thermal Skin Effect. *Deep. Sea Res. Part II Top. Stud. Oceanogr.* **2011**, *58*, 861–868. [CrossRef]
35. Hulley, G.C.; Hook, S.J. *ECOSTRESS Level-2 Cloud Detection Algorithm Theoretical Basis Document (ATBD)*; Jet Propulsion Laboratory: Pasadena, CA, USA, 2018. Available online: https://lpdaac.usgs.gov/documents/296/ECO2_Cloud_ATBD_V1.pdf (accessed on 22 May 2024).
36. Walton, C.C.; Sullivan, J.T.; Rao, C.R.N.; Weinreb, M.P. Corrections for Detector Nonlinearities and Calibration Inconsistencies of the Infrared Channels of the Advanced Very High Resolution Radiometer. *J. Geophys. Res.* **1998**, *103*, 3323–3337. [CrossRef]
37. Theocharous, E.; Ishii, J.; Fox, N.P. Absolute Linearity Measurements on HgCdTe Detectors in the Infrared Region. *Appl. Opt.* **2004**, *43*, 4182. [CrossRef] [PubMed]
38. Theocharous, E.; Theocharous, O.J. Practical Limit of the Accuracy of Radiometric Measurements Using HgCdTe Detectors. *Appl. Opt.* **2006**, *45*, 7753. [CrossRef] [PubMed]
39. Arai, K.; Tonooka, H. Radiometric Performance Evaluation of ASTER VNIR, SWIR, and TIR. *IEEE Trans. Geosci. Remote Sens.* **2005**, *43*, 2725–2732. [CrossRef]
40. Mittaz, J.P.D.; Harris, A.R.; Sullivan, J.T. A Physical Method for the Calibration of the AVHRR/3 Thermal IR Channels 1: The Prelaunch Calibration Data. *J. Atmos. Ocean. Technol.* **2009**, *26*, 996–1019. [CrossRef]
41. Mittaz, J.; Harris, A. A Physical Method for the Calibration of the AVHRR/3 Thermal IR Channels. Part II: An In-Orbit Comparison of the AVHRR Longwave Thermal IR Channels on Board MetOp-A with IASI. *J. Atmos. Ocean. Technol.* **2011**, *28*, 1072–1087. [CrossRef]
42. Chang, T.; Wu, X.; Weng, F. Modeling Thermal Emissive Bands Radiometric Calibration Impact with Reference to AVHRR. *J. Geophys. Res. Atmos.* **2017**, *122*, 2831–2843. [CrossRef]
43. Sakuma, F.; Ono, A.; Tsuchida, S.; Ohgi, N.; Inada, H.; Akagi, S.; Ono, H. Onboard Calibration of the ASTER Instrument. *IEEE Trans. Geosci. Remote Sens.* **2005**, *43*, 2715–2724. [CrossRef]
44. Tonooka, H.; Sakuma, F.; Tachikawa, T.; Kikuchi, M. Radiometric Calibration Status and Recalibration of Aster Thermal Infrared Images. In Proceedings of the IGARSS 2019—2019 IEEE International Geoscience and Remote Sensing Symposium, Yokohama, Japan, 28 July–2 August 2019; IEEE: New York, NY, USA, 2019; pp. 8530–8533. [CrossRef]
45. Smith, D.; Barillot, M.; Bianchi, S.; Brandani, F.; Coppo, P.; Etxaluze, M.; Frerick, J.; Kirschstein, S.; Lee, A.; Maddison, B.; et al. Sentinel-3A/B SLSTR Pre-Launch Calibration of the Thermal InfraRed Channels. *Remote Sens.* **2020**, *12*, 2510. [CrossRef]
46. Xiong, X.; Butler, J.J. MODIS and VIIRS Calibration History and Future Outlook. *Remote Sens.* **2020**, *12*, 2523. [CrossRef]
47. Cao, C.; Wang, W.; Blonski, S.; Zhang, B. Radiometric Traceability Diagnosis and Bias Correction for the Suomi NPP VIIRS Long-wave Infrared Channels during Blackbody Unsteady States. *JGR Atmos.* **2017**, *122*, 5285–5297. [CrossRef]

48. Efremova, B.; McIntire, J.; Moyer, D.; Wu, A.; Xiong, X. S-NPP VIIRS Thermal Emissive Bands on-Orbit Calibration and Performance. *J. Geophys. Res. Atmos.* **2014**, *119*, 10859–10875. [CrossRef]
49. Pérez Díaz, C.L.; Xiong, X.; Li, Y.; Chiang, K. S-NPP VIIRS Thermal Emissive Bands 10-Year On-Orbit Calibration and Performance. *Remote Sens.* **2021**, *13*, 3917. [CrossRef]
50. Logan, T.L.; Johnson, W.R. *ECOSTRESS Level-1 Focal Plane Array and Radiometric Calibration Algorithm Theoretical Basis Document*; Jet Propulsion Laboratory: Pasadena, CA, USA, 2018. Available online: https://lpdaac.usgs.gov/documents/222/ECO1B_Calibration_ATBD_V1.pdf (accessed on 22 May 2024).
51. Johnson, W.R.; Hook, S.J.; Schmitigal, W.; Goullioud, R. ECOSTRESS End-to-End Radiometric Pre-Flight Calibration and Validation. In Proceedings of the SPIE Optical Engineering + Applications, San Diego, CA, USA, 19–23 August 2018. [CrossRef]
52. Smyth, M.M.; Logan, T.L. *ECOSTRESS Level 1 Product User Guide Version 3*; Jet Propulsion Laboratory: Pasadena, CA, USA, 2022. Available online: https://lpdaac.usgs.gov/documents/1491/ECO1B_User_Guide_V2.pdf (accessed on 22 May 2024).
53. Johnson, W. ECOSTRESS Lab Performance. In Proceedings of the HyspIRI Workshop, Pasadena, CA, USA, 19 October 2016; Available online: https://hyspiri.jpl.nasa.gov/downloads/2016_Workshop/day2/14_161019-ECOSTRESS_Lab_Performance_3.pdf (accessed on 22 May 2024).
54. Smyth, M.; Leprince, S. *ECOSTRESS Level-1B Resampling and Geolocation Algorithm Theoretical Basis Document (ATBD)*; Jet Propulsion Laboratory: Pasadena, CA, USA, 2018. Available online: https://lpdaac.usgs.gov/223/ECO1B_Geolocation_ATBD_V1.pdf (accessed on 22 May 2024).
55. Krehbiel, K. ECOSTRESS Swath to Grid Conversion Script. Available online: https://git.earthdata.nasa.gov/projects/LPDUR/repos/ecostress_swath2grid/browse (accessed on 17 March 2024).
56. Buffet, L.; Gamet, P.; Maisongrande, P.; Salcedo, C.; Crebassol, P. The TIR Instrument on TRISHNA Satellite: A Precursor of High Resolution Observation Missions in the Thermal Infrared Domain. In Proceedings of the International Conference on Space Optics—ICSO 2020, Virtual Conference, 30 March–2 April 2021; Cugny, B., Sodnik, Z., Karafolas, N., Eds.; SPIE: Bellingham, WA, USA, 2021; p. 118520. Available online: https://www.spiedigitallibrary.org/conference-proceedings-of-spie/11852/2599173/The-TIR-instrument-on-TRISHNA-satellite--a-precursor-of/10.1117/12.2599173.full (accessed on 22 May 2024).
57. Cawse-Nicholson, K.; Townsend, P.A.; Schimel, D.; Assiri, A.M.; Blake, P.L.; Buongiorno, M.F.; Campbell, P.; Carmon, N.; Casey, K.A.; Correa-Pabón, R.E.; et al. NASA's Surface Biology and Geology Designated Observable: A Perspective on Surface Imaging Algorithms. *Remote Sens. Environ.* **2021**, *257*, 112349. [CrossRef]
58. Koetz, B.; Bastiaanssen, W.; Berger, M.; Defourney, P.; Del Bello, U.; Drusch, M.; Drinkwater, M.; Duca, R.; Fernandez, V.; Ghent, D.; et al. High Spatio-Temporal Resolution Land Surface Temperature Mission—A Copernicus Candidate Mission in Support of Agricultural Monitoring. In Proceedings of the IGARSS 2018—2018 IEEE International Geoscience and Remote Sensing Symposium, Valencia, Spain, 22–27 July 2018; IEEE: Bellingham, WA, USA, 2018; pp. 8160–8162. [CrossRef]
59. Xu, F.; Ignatov, A. Error Characterization in *i*Quam SSTs Using Triple Collocations with Satellite Measurements. *Geophys. Res. Lett.* **2016**, *43*, 10826–10834. [CrossRef]
60. Xu, F.; Ignatov, A. iQuam In Situ SST Quality Monitor v2.10. Available online: https://www.star.nesdis.noaa.gov/socd/sst/iquam/data.html (accessed on 18 March 2024).
61. LPDAAC ECOSTRESS Brightness Temperature Lookup Tables. Available online: https://git.earthdata.nasa.gov/projects/LPDUR/repos/ecostress_swath2grid/browse/EcostressBrightnessTemperatureV01.h5 (accessed on 17 March 2024).
62. European Centre for Medium-Range Weather Forecasts ERA5 Reanalysis (0.25 Degree Latitude-Longitude Grid). Available online: https://doi.org/10.5065/BH6N-5N20 (accessed on 17 March 2024).
63. Saunders, R.; Hocking, J.; Rundle, D.; Rayer, P.; Havemann, S.; Matricardi, M.; Geer, A.; Lupu, C.; Brunel, P.; Vidot, J. *RTTOV-12 Science and Validation Report*; Eumetsat NWP SAF: Reading, UK, 2017; Available online: https://nwp-saf.eumetsat.int/site/download/documentation/rtm/docs_rttov12/rttov12_svr.pdf (accessed on 22 May 2024).
64. Donlon, C.J.; Minnett, P.J.; Gentemann, C.; Nightingale, T.J.; Barton, I.J.; Ward, B.; Murray, M.J. Toward Improved Validation of Satellite Sea Surface Skin Temperature Measurements for Climate Research. *J. Clim.* **2002**, *15*, 353–369. [CrossRef]
65. Liang, X.; Ignatov, A. Monitoring of IR Clear-Sky Radiances over Oceans for SST (MICROS). *J. Atmos. Ocean. Technol.* **2011**, *28*, 1228–1242. [CrossRef]
66. Liberti, G.L.; Sabatini, M.; Wethey, D.S.; Ciani, D. A Multi-Pixel Split-Window Approach to Sea Surface Temperature Retrieval from Thermal Imagers with Relatively High Radiometric Noise: Preliminary Studies. *Remote Sens.* **2023**, *15*, 2453. [CrossRef]
67. Von Neumann, J. Distribution of the Ratio of the Mean Square Successive Difference to the Variance. *Ann. Math. Statist.* **1941**, *12*, 367–395. [CrossRef]
68. R Core Team. R: A Language and Environment for Statistical Computing. Available online: https://www.R-project.org (accessed on 22 May 2024).
69. RStudio Team. RStudio: Integrated Development for R. Available online: https://www.posit.co (accessed on 22 May 2024).
70. Pierce, D. Ncdf4: Interface to Unidata netCDF (Version 4 or Earlier) Format Data. Available online: https://CRAN.R-project.org/package=ncdf4 (accessed on 23 March 2024).
71. Fischer, B.; Smith, M.; Pau, G. Rhdf5: R Interface to HDF5. Available online: https://doi.org/10.18129/B9.bioc.rhdf5 (accessed on 22 May 2024).
72. Ooms, J. Sys: Powerful and Reliable Tools for Running System Commands in R. Available online: https://CRAN.R-project.org/package=sys (accessed on 23 March 2024).

73. Schmidt, D.; Chen, W. getPass: Masked User Input. Available online: https://cran.r-project.org/package=getPass (accessed on 22 May 2024).
74. Wickham, H. Httr: Tools for Working with Urls and Http. Available online: https://CRAN.R-project.org/package=httr (accessed on 23 March 2023).
75. Wickham, H.; Henry, L. Purrr: Functional Programming Tools. Available online: https://CRAN.R-project.org/package=purrr (accessed on 23 March 2024).
76. Wickham, H. Rvest: Easily Harvest (Scrape) Web Pages. Available online: https://CRAN.R-project.org/package=rvest (accessed on 23 March 2024).
77. Wickham, H.; François, R.; Henry, L.; Müller, K.; Vaughan, D. Dplyr: A Grammar of Data Manipulation. Available online: https://CRAN.R-project.org/package=dplyr (accessed on 23 March 2024).
78. Plate, T.; Heiberger, R. Abind: Combine Multidimensional Arrays. Available online: https://CRAN.R-project.org/package=abind (accessed on 23 March 2024).
79. Hiebert, J. Udunits2: Udunits-2 Bindings for R. Available online: https://CRAN.R-project.org/package=udunits2 (accessed on 22 May 2024).
80. Lai, R. Retry: Repeated Evaluation. Available online: https://CRAN.R-project.org/package=retry (accessed on 23 March 2024).
81. Hijmans, R.J. Terra: Spatial Data Analysis. Available online: https://CRAN.R-project.org/package=terra (accessed on 23 March 2024).
82. Arya, S.; Mount, D.; Kemp, S.E.; Jefferis, G. RANN: Fast Nearest Neighbour Search (Wraps ANN Library) Using L2 Metric. Available online: https://CRAN.R-project.org/package=RANN (accessed on 23 March 2024).
83. Pebesma, E.; Bivand, R. Sp: Classes and Methods for Spatial Data in R. Available online: https://CRAN.R-project.org/package=sp (accessed on 23 March 2024).
84. Baddeley, A.; Rubak, E.; Turner, R. Spatstat: An R Package for Analyzing Spatial Point Patterns. Available online: https://CRAN.R-project.org/package=spatstat (accessed on 23 March 2024).
85. Dutky, S.; Maechler, M. Bitops: Bitwise Operations. Available online: https://CRAN.R-project.org/package=bitops (accessed on 23 March 2024).
86. Chau, J. Gslnls: GSL Nonlinear Least Squares Fitting. Available online: https://CRAN.R-project.org/package=gslnls (accessed on 23 March 2024).
87. Pierre-Jean, M.; Gigaill, G.; Neuvial, P. Jointseg: Joint Segmentation of Multivariate (Copy Number) Signals. Available online: https://CRAN.R-project.org/package=jointseg (accessed on 23 March 2024).
88. Signorell, A. DescTools: Tools for Descriptive Statistics. Available online: https://CRAN.R-project.org/package=DescTools (accessed on 23 March 2024).
89. Wickham, H. Ggplot2: Elegant Graphics for Data Analysis. Available online: https://ggplot2.tidyverse.org (accessed on 23 March 2024).
90. Garnier, S.; Ross, N.; Rudis, R.; Camargo, A.P.; Sciaini, M.; Scherer, C. Viridis: Colorblind-Friendly Color Maps for R. Available online: https://cran.r-project.org/package=viridis (accessed on 23 March 2024).
91. Kassambara, A. Ggpubr: "ggplot2" Based Publication Ready Plots. Available online: https://CRAN.R-project.org/package=ggpubr (accessed on 23 March 2024).
92. NOAA SST Quality Monitor. Available online: https://www.star.nesdis.noaa.gov/socd/sst/squam/index.php (accessed on 5 April 2024).
93. Baldridge, A.M.; Hook, S.J.; Grove, C.I.; Rivera, G. The ASTER Spectral Library Version 2.0. *Remote Sens. Environ.* **2009**, *113*, 711–715. [CrossRef]
94. Padula, F.; Cao, C. Detector-Level Spectral Characterization of the Suomi National Polar-Orbiting Partnership Visible Infrared Imaging Radiometer Suite Long-Wave Infrared Bands M15 and M16. *Appl. Opt.* **2015**, *54*, 5109. [CrossRef] [PubMed]
95. Wang, Z.; Cao, C. Assessing the Effects of Suomi NPP VIIRS M15/M16 Detector Radiometric Stability and Relative Spectral Response Variation on Striping. *Remote Sens.* **2016**, *8*, 145. [CrossRef]
96. Oudrari, H.; McIntire, J.; Xiong, X.; Butler, J.; Ji, Q.; Schwarting, T.; Lee, S.; Efremova, B. JPSS-1 VIIRS Radiometric Characterization and Calibration Based on Pre-Launch Testing. *Remote Sens.* **2016**, *8*, 41. [CrossRef]
97. Lin, L.; Cao, C. The Effects of VIIRS Detector-Level and Band-Averaged Relative Spectral Response Differences Between S-NPP and NOAA-20 on the Thermal Emissive Bands. *IEEE J. Sel. Top. Appl. Earth Obs. Remote Sens.* **2019**, *12*, 4123–4130. [CrossRef]
98. Jau, B.M.; Hook, S.J.; Johnson, W.R.; Foote, M.C.; Paine, C.G.; Pannell, Z.W.; Smythe, R.F.; Kuan, G.M.; Jablonski, J.K.; Eng, B.T. *PHyTIR-A Prototype Thermal Infrared Radiometer*; IEEE: Big Sky, MT, USA, 2013; Available online: https://hdl.handle.net/2014/44954 (accessed on 22 May 2024).
99. Wang, W.; Cao, C. NOAA-20 and S-NPP VIIRS Thermal Emissive Bands On-Orbit Calibration Algorithm Update and Long-Term Performance Inter-Comparison. *Remote Sens.* **2021**, *13*, 448. [CrossRef]
100. Smith, D.; Hunt, S.E.; Etxaluze, M.; Peters, D.; Nightingale, T.; Mittaz, J.; Woolliams, E.R.; Polehampton, E. Traceability of the Sentinel-3 SLSTR Level-1 Infrared Radiometric Processing. *Remote Sens.* **2021**, *13*, 374. [CrossRef]
101. Madhavan, S.; Xiong, X.; Wu, A.; Wenny, B.N.; Chiang, K.; Chen, N.; Wang, Z.; Li, Y. Noise Characterization and Performance of MODIS Thermal Emissive Bands. *IEEE Trans. Geosci. Remote Sens.* **2016**, *54*, 3221–3234. [CrossRef] [PubMed]

102. Bouali, M.; Ignatov, A. Estimation of Detector Biases in MODIS Thermal Emissive Bands. *IEEE Trans. Geosci. Remote Sens.* **2013**, *51*, 4339–4348. [CrossRef]
103. Charvet, D.; Gnata, X.; Toulemont, A.; Rizzolo, S.; Clénet, A.; Libouban, C.; Gossant, A.; Chassat, F.; Buffet, L.; Salcedo, C.; et al. TRISHNA TIR Instrument Development and Performance Status. In Proceedings of the ICSO 2022, Dubrovnik, Croatia, 3–7 October 2022; SPIE: Bellingham, WA, USA, 2022; Volume 12777, p. 1277742. [CrossRef]
104. Basilio, R.R.; Hook, S.J.; Zoffoli, S.; Buongiorno, M.F. Surface Biology and Geology (SBG) Thermal Infrared (TIR) Free-Flyer Concept. In Proceedings of the 2022 IEEE Aerospace Conference (AERO), Big Sky, MT, USA, 5–12 March 2022; IEEE: Big Sky, MT, USA, 2022; pp. 1–9. [CrossRef]
105. Bernard, F.; Bourgeois, G.; Manolis, I.; Barat, I.; Alamanac, A.B.; Taboada, M.S.; Mingorance, P.; Ciapponi, A.; Cardone, T.; Dutruel, E.; et al. The LSTM Instrument: Design, Technology and Performance. In Proceedings of the International Conference on Space Optics—ICSO 2022, Dubrovnik, Croatia, 3–7 October 2022; Minoglou, K., Karafolas, N., Cugny, B., Eds.; SPIE: Bellingham, WA, USA, 2023; p. 144. [CrossRef]
106. Smith, D.; Mutlow, C.; Delderfield, J.; Watkins, B.; Mason, G. ATSR Infrared Radiometric Calibration and In-Orbit Performance. *Remote Sens. Environ.* **2012**, *116*, 4–16. [CrossRef]
107. Xiong, X.; Wenny, B.N.; Wu, A.; Barnes, W.L. MODIS Onboard Blackbody Function and Performance. *IEEE Trans. Geosci. Remote Sens.* **2009**, *47*, 4210–4222. [CrossRef]
108. Mason, I.M.; Sheather, P.H.; Bowles, J.A.; Davies, G. Blackbody Calibration Sources of High Accuracy for a Spaceborne Infrared Instrument: The Along Track Scanning Radiometer. *Appl. Opt.* **1996**, *35*, 629. [CrossRef] [PubMed]
109. Maple Version 15.01. Available online: https://www.maplesoft.com (accessed on 23 March 2024).